Optimal Transport from Wall to Wall

Pedram Hassanzadeh

October 3, 2012

1 Introduction

Transport of heat and mass is of fundamental importance in science and engineering. In some environmental and industrial applications, the aim is to maximize (e.g. in cooling or heating) or minimize (e.g. for pollution and hazards) the transport. In some other problems, such as oil spills, the amount and the path of the transported material must be determined. For problems arising in nature, the focus is on understanding the transport processes and estimating their magnitude. In some problems with extreme parameters, such as mantle convection, the interest is mainly on finding scaling laws relating the magnitude of the transport to some physical parameters.

The focus of this investigation is a generic question: what is the maximum amount of a passive scalar tracer that can be transported by unknown velocity fields satisfying certain constraints. The constraints studied here are that the velocity field is divergence–free and has a fixed (given) amount of (kinetic) energy or a fixed amount of enstrophy. Subsequently, we shall discuss the motivation inspiring these constraints. Furthermore, we restrict our attention to two–dimensional (2D) steady flows.

In the remainder of the Introduction, we will present details of the problem and its mathematical formulation. In sections 2 and 3, we study the problems with fixed energy and fixed enstrophy, respectively. For each problem, we employ the calculus of variations to maximize a functional subjected to the constraints of the problem. The resulting Euler–Lagrange equations are solved numerically and analytically to obtain the optimal velocity field. Upper bounds on the transport are calculated from the optimal velocity fields. At the end of each section, the calculated upper bound is compared with the available results for relevant problems. Section 4 presents the concluding remarks and future work.

1.1 Mathematical Formulation

Here we present the mathematical formulation of the problem described above. For convenience, we only consider heat transport (i.e. with temperature treated as scalar tracer) hereafter. The 2D heat transport is described by the advection-diffusion equation:

$$\dot{T} + \mathbf{v} \cdot \nabla T = \kappa \Delta T, \tag{1}$$

where $T(x, z, t)$ is temperature, $\dot{T} = \partial T/\partial t$, $\Delta = \partial^2/\partial x^2 + \partial^2/\partial z^2$, κ is the thermal diffusivity of the fluid (assumed to be constant), and $\mathbf{v}(x, z, t) = (u, w)$ is the divergence–free

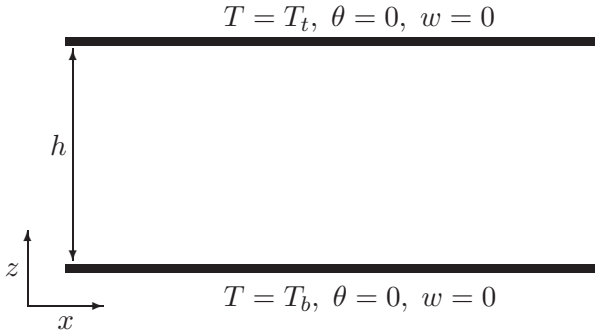

Figure 1: Schematic of the configuration. The top and bottom walls are impermeable and are kept at fixed temperatures.

velocity field, i.e.

$$\nabla \cdot \mathbf{v} = 0. \tag{2}$$

In the absence of advection (i.e. $\mathbf{v} = 0$), the transport is purely by conduction and the temperature field of this case is denoted by Θ. $\theta \equiv T - \Theta$ is the deviation of the temperature field from the purely conducting profile Θ when $\mathbf{v} \neq 0$. The geometry of the problem, shown in Figure 1, consists of two infinite parallel impermeable walls with fixed temperature. Note that the parallel walls can be horizontal or vertical or inclined; we do not use the dynamics of the velocity field (i.e. momentum equations) in our analysis and therefore gravity is irrelevant. We set the walls to be horizontal. The flow is assumed to be periodic in the x direction with characteristic horizontal length scale L, which will be specified later.

In the next two sections, we study velocity fields that either have fixed energy U^2,

$$U^2 = \frac{1}{hL}\int_D (\mathbf{v}\cdot\mathbf{v})\,\mathrm{d}x\mathrm{d}z, \tag{3}$$

or fixed enstrophy Ω^2,

$$\Omega^2 = \frac{1}{hL}\int_D (\boldsymbol{\omega}\cdot\boldsymbol{\omega})\,\mathrm{d}x\mathrm{d}z = \frac{1}{hL}\int_D (\nabla\mathbf{v} : \nabla\mathbf{v})\,\mathrm{d}x, \tag{4}$$

where $\boldsymbol{\omega} = \nabla \times \mathbf{v}$ is the vorticity, and D is the $[0, L] \times [0, h]$ domain. The second equality in (4) is true for many boundary conditions including no–slip, free–slip, and periodic. The significance of the second integral is that, multiplied by viscosity, it gives the viscous dissipation rate in Newtonian fluids. As the integrals are equal for the boundary conditions of interest, we use the second representation in this report because it is more convenient.

We non-dimensionalize length with the spacing between the walls h, time with diffusion time scale h^2/κ, and velocity with κ/h. The dimensionless temperature is $(T - T_t)/(T_b - T_t)$. We define the (dimensionless) Pećlet number Pe as the ratio of the diffusive time scale to the advective time scale (i.e. a measure of the strength of advection relative to diffusion). For the problem with fixed energy,

$$\mathrm{Pe} \equiv Uh/\kappa, \tag{5}$$

and for the problem with fixed enstrophy,

$$\mathrm{Pe} \equiv \Omega h^2/\kappa. \tag{6}$$

We also define the aspect ratio Γ as

$$\Gamma \equiv L/h. \tag{7}$$

Notice that hereafter all variables (i.e. $\mathbf{v}$, T, Θ, θ, x, z, t) are dimensionless, but the notation is not changed for simplicity.

Non-dimensionalizing equations (1)–(2) and the boundary conditions yields

$$\begin{aligned} \dot{\theta} + \mathbf{v}\cdot\nabla\theta &= \Delta\theta + w, && (8)\\ \nabla\cdot\mathbf{v} &= 0, && (9)\\ \theta(x,0,t) &= \theta(x,1,t) = 0, && (10)\\ w(x,0,t) &= w(x,1,t) = 0, && (11) \end{aligned}$$

where $\theta(x,z,t) \equiv T(x,z,t) - \Theta(z)$ has been used (note that $\Theta(z) = 1 - z$).

We further define angle brackets $\langle\cdot\rangle$ as the long time–space average:

$$\langle \boldsymbol{a}(x,z,t)\rangle \equiv \lim_{t\to\infty}\frac{1}{t}\int_0^t \left\{\frac{1}{\Gamma}\int_D \boldsymbol{a}(x,z,s)\,\mathrm{d}x\mathrm{d}z\right\}\mathrm{d}s, \quad D = [0,1]\times[0,\Gamma]. \tag{12}$$

Therefore, using (5), the fixed energy constraint (3) becomes

$$\mathrm{Pe} = \left\langle |\mathbf{v}|^2 \right\rangle. \tag{13}$$

The fixed enstrophy constraint (4) is

$$\mathrm{Pe} = \left\langle |\nabla\mathbf{v}|^2 \right\rangle, \tag{14}$$

where (6) has been used.

The Nusselt number Nu measures the heat transport by advection and is defined as the ratio of the heat flux in the *presence* of advection $\mathbf{q}_\mathrm{a}$ to the heat flux by pure conduction $\mathbf{q}_\mathrm{c}$. We are interested in the vertical transport between horizontal walls, therefore

$$\mathrm{Nu} \equiv \frac{\langle \mathbf{q}_\mathrm{a}\cdot\mathbf{z}\rangle}{\langle \mathbf{q}_\mathrm{c}\cdot\mathbf{z}\rangle}, \tag{15}$$

where $\mathbf{q}_\mathrm{c} = -\nabla\Theta$ (Fourier's law) and $\mathbf{q}_\mathrm{a} = -\nabla T + T\mathbf{v}$. Hence, after a little algebra, the above equation reduces to

$$\mathrm{Nu} = 1 + \langle wT\rangle = 1 + \langle w\theta\rangle. \tag{16}$$

Note that $\langle w\Theta(z)\rangle = 0$ as a result of incompressibility.

1.2 Objective

With the strength of advection (Pe), geometry of the flow (Γ), and strength of transport (Nu) defined, we can now rigorously present the goal of this work.

1. We search over all divergence–free velocity fields $\mathbf{v}$ that have a given (Pe, Γ) (and satisfy (11)), and find the maximum possible Nu (16) (notice that knowing $\mathbf{v}$, (10) and (8) uniquely determine θ). This Nu is called $\mathrm{Nu}_{\max}$:
$$\mathrm{Nu}_{\max}(\mathrm{Pe}, \Gamma) \equiv \sup_{\mathbf{v}} \{\mathrm{Nu}(\mathbf{v})\}. \tag{17}$$
2. For the same Pe, step 1 is repeated for various values of Γ. For this Pe, the largest value of $\mathrm{Nu}_{\max}(\mathrm{Pe}, \Gamma)$ is called $\mathrm{Nu}_{\mathrm{MAX}}$:
$$\mathrm{Nu}_{\mathrm{MAX}}(\mathrm{Pe}) \equiv \sup_{\Gamma} \{\mathrm{Nu}_{\max}(\mathrm{Pe}, \Gamma)\}. \tag{18}$$
3. For this Pe, the Γ in step 2 which gives $\mathrm{Nu}_{\mathrm{MAX}}$ is dubbed the optimal aspect ratio and noted as $\Gamma_{\mathrm{opt}}(\mathrm{Pe})$

The goal is to find $\mathrm{Nu}_{\max}(\mathrm{Pe}, \Gamma)$, $\mathrm{Nu}_{\mathrm{MAX}}(\mathrm{Pe})$, and $\Gamma_{\mathrm{opt}}(\mathrm{Pe})$ for any Pe, especially in the limit of $\mathrm{Pe} \to \infty$. In sections 2.5 and 3.4 we show how to interpret the results based on the Rayleigh number Ra commonly arising in buoyancy–driven convection problems.

The time–dependence of the advecting flow merits further discussion. The effect of unsteadiness on transport is not fully understood and whether a time-dependent flow transports more or less than a steady flow (with the same amount of energy or enstrophy) remains an open question. Of course the question can be answered by performing the optimization in step 1 over both space and time, i.e. for $\mathbf{v} = \mathbf{v}(x, z, t)$. Such an analysis is very complicated and is a problem of optimal control theory. Here we focus on steady flows (i.e. $\mathbf{v} = \mathbf{v}(x, z)$) and use calculus of variations in step 1. The steady analysis gives useful insight into the optimal transport problem that can be used to guide future unsteady analyses.

2 Optimal Transport with Fixed Energy

In the first problem, we look into the optimal steady transport with fixed energy. Therefore, equations (8)–(11) and (13) become

$$\begin{aligned}
\mathbf{v} \cdot \nabla\theta &= \Delta\theta + w, && (19)\\
\nabla \cdot \mathbf{v} &= 0, && (20)\\
\mathrm{Pe} &= \left\langle |\mathbf{v}|^2 \right\rangle, && (21)\\
\theta(x,0) &= \theta(x,1) = 0, && (22)\\
w(x,0) &= w(x,1) = 0. && (23)
\end{aligned}$$

A simple analysis gives a relatively crude upper bound on Nu as $1 + \mathrm{Pe}/2$. Starting from (16),

$$\begin{aligned}
\mathrm{Nu} &= 1 + \langle wT \rangle = 1 + \langle w(T - 1/2) \rangle \le 1 + \left\langle |w|^2 \right\rangle^{1/2} \left\langle |T - 1/2|^2 \right\rangle^{1/2} \le 1 + \frac{\left\langle |\mathbf{v}|^2 \right\rangle^{1/2}}{2} \\
&= 1 + \frac{\mathrm{Pe}}{2}, && (24)
\end{aligned}$$

where the second equality is due to incompressibility and the boundary conditions. The Cauchy–Schwarz inequality has been used in the first inequality. The maximum principle assures $|T| \leq 1$ and consequently $|T - 1/2| \leq 1/2$. The latter has been used in the second inequality. Equation (21) gives the final result. This upper bound, as shown later, is too high, and a full analysis of (19)–(23), as given below, is required to obtain a better estimate, and to find the optimal velocity field.

2.1 Variational Formulation for Steady Flows

Here the variational formulation is presented to maximize $\mathrm{Nu} = 1 + \langle \theta w \rangle$ given constraints (19)-(21) and boundary conditions (22)-(23). Therefore, we aim to maximize the functional $\mathcal{F}$ constructed as

$$\mathcal{F} = \left\langle w\theta - \phi(x,z)\left(\mathbf{v}\cdot\nabla\theta - \Delta\theta - w\right) + p(x,z)\left(\nabla\cdot\mathbf{v}\right) - \frac{\mu}{2}\left(|\mathbf{v}|^2 - \mathrm{Pe}^2\right)\right\rangle \tag{25}$$

where $\phi(x,z)$, $p(x,z)$, and μ are Lagrange multipliers (ϕ and p are functions of x and z to enforce the constraints (19) and (20) point-wise). The Euler-Lagrange equations can be expressed as [2]:

$$0 = \frac{\delta\mathcal{F}}{\delta\mathbf{v}} = (\theta+\phi)\,\hat{\boldsymbol{z}} + \theta\,\nabla\phi - \nabla p - \mu\mathbf{v}, \tag{26}$$

$$0 = \frac{\delta\mathcal{F}}{\delta\theta} = \mathbf{v}\cdot\nabla\phi + \Delta\phi + w, \tag{27}$$

$$0 = \frac{\delta\mathcal{F}}{\delta\phi} = \mathbf{v}\cdot\nabla\theta - \Delta\theta - w, \tag{28}$$

$$0 = \frac{\delta\mathcal{F}}{\delta p} = \nabla\cdot\mathbf{v}, \tag{29}$$

$$0 = \frac{\partial\mathcal{F}}{\partial\mu} = \left\langle|\mathbf{v}|^2\right\rangle - \mathrm{Pe}^2, \tag{30}$$

where $\nabla\cdot\mathbf{v} = 0$ and integration by parts along with boundary conditions (22)-(23) and periodicity in the x direction have been repeatedly employed to derive (26) and (27). Additionally, in deriving (27), it has been assumed that ϕ vanishes at $z = [0,1]$ (to eliminate a surface term arising from the integration by parts of $\phi\Delta\theta$, i.e. natural boundary conditions). Therefore the boundary conditions are

$$w(x,0) = w(x,1) = 0, \tag{31}$$

$$\theta(x,0) = \theta(x,1) = 0, \tag{32}$$

$$\phi(x,0) = \phi(x,1) = 0. \tag{33}$$

Also notice that using integration by parts, the $+\theta\,\nabla\phi$ term in (26) can be replaced by $-\phi\,\nabla\theta$ (since $\nabla(\theta\phi)$ is a perfect gradient and can be absorbed into the ∇p term). As expected for an incompressible flow, the Lagrange multiplier enforcing $\nabla\cdot\mathbf{v} = 0$ in equation (25) (i.e. p), plays a role similar to *pressure* in the resulting equations.

Inspection of equations (26) and (28)-(29) reveals some similarities between these equations and the equations of convection in porous media in the limit of infinite Prandtl-Darcy number (see e.g. [6]), although here, an extra field ϕ exists. This resemblance, which will also be observed in the linear analysis in the next section, will be discussed in section 2.5.

2.2 The Limit of Small Pe: Asymptotic Solution

In the limit of small Pe, $|\mathbf{v}| \ll 1$ (from (30)), which along with (27)-(28) and the maximum principle imply that $|\theta| \ll 1$ and $|\phi| \ll 1$. Therefore in this limit we can linearize equations (26)-(28):

$$\begin{aligned} \mu\,\mathbf{v} + \nabla p &= (\theta + \phi)\hat{\boldsymbol{z}}, && (34)\\ \Delta\phi + w &= 0, && (35)\\ \Delta\theta + w &= 0, && (36)\\ \nabla \cdot \mathbf{v} &= 0. && (37) \end{aligned}$$

Subtracting (36) from (35) and using (32)-(33) gives $\theta = \phi$ in the small Pe regime. Taking the divergence of equation (34) gives

$$\Delta p = 2\,\theta_z, \tag{38}$$

where the subscript z means $\partial/\partial z$. Taking Δ of the $\hat{\boldsymbol{z}}$-component of (34) results in

$$\mu\Delta w + \Delta p_z = 2\,\Delta\theta. \tag{39}$$

Subtracting $\partial/\partial z$ of (38) from (39) gives

$$\mu\Delta w = 2\,\theta_{xx}, \tag{40}$$

which along with equation (36) and boundary conditions (31)-(32) can be analytically solved to find ($\mathbf{v}$,θ) in the small–Pe limit. A Fourier transform in the x direction, these equations become

$$\begin{aligned} (D_z^2 - k^2)\,\hat{\theta}_k(z) + \hat{w}_k(z) &= 0, && (41)\\ \mu(D_z^2 - k^2)\,\hat{w}_k(z) + 2k^2\,\hat{\theta}_k(z) &= 0, && (42) \end{aligned}$$

where $D_z = \partial/\partial z$. $\hat{w}_k(z)$ and $\hat{\theta}_k(z)$ are the Fourier coefficients of w and θ with horizontal wavenumber k. Defining L as half of the (dimensionless) wavelength, we see that $\Gamma = \pi/k$. Given the form of these equations and the boundary conditions, the solution is

$$\begin{aligned} \hat{w}_k(z) &= A_k\,\sin(m\pi z), && (43)\\ \hat{\theta}_k(z) &= B_k\,\sin(m\pi z), && (44) \end{aligned}$$

where m is the vertical wavenumber, and A_k and B_k are still undetermined. Substituting into (41) and (42) gives

$$\begin{aligned} \mu &= (2\,k^2)/(m^2\pi^2 + k^2)^2, && (45)\\ A_k &= (m^2\pi^2 + k^2)\,B_k. && (46) \end{aligned}$$

Using equation (37), $\hat{u}_k(z)$ is obtained as

$$\hat{u}_k(z) = i\,\frac{m\pi}{k}\,A_k\,\cos(m\pi z). \tag{47}$$

Substituting (47) and (43) into (30) yields

$$\left\langle |\mathbf{v}|^2 \right\rangle = \left(A_k^2 + \frac{m^2\pi^2}{k^2} A_k^2 \right) = \mathrm{Pe}^2 \Rightarrow A_k = \frac{k}{(m^2\pi^2 + k^2)^{1/2}} \mathrm{Pe}, \tag{48}$$

which along with (46) gives

$$B_k = \frac{k}{(m^2\pi^2 + k^2)^{3/2}} \mathrm{Pe}. \tag{49}$$

Knowing A_k and B_k, Nu is obtained from (16):

$$\mathrm{Nu} = 1 + A_k B_k = 1 + \frac{k^2}{(m^2\pi^2 + k^2)^2} \mathrm{Pe}^2, \tag{50}$$

which for a given $(\mathrm{Pe}, \Gamma = \pi/k)$, is maximized at $m = 1$. As a result, using the notation defined in section 1.2:

$$\mathrm{Nu}_{\max}(\mathrm{Pe}, \Gamma) = 1 + \frac{\Gamma^2}{\pi^2(\Gamma^2 + 1)^2} \mathrm{Pe}^2. \tag{51}$$

The largest value of $\mathrm{Nu}_{\max}(\mathrm{Pe}, \Gamma)$, i.e. $\mathrm{Nu}_{\mathrm{MAX}}$, is achieved at $\Gamma_{\mathrm{opt}} = 1$:

$$\mathrm{Nu}_{\mathrm{MAX}}(\mathrm{Pe}) = 1 + \frac{\mathrm{Pe}^2}{4\pi^2} \tag{52}$$

Notice that $(k, m) = (\pi, 1)$ corresponds to the maximum value of $\mu = 1/(2\pi)^2$ (see (45)). Therefore, in the limit of small Pe (i.e. large μ), the maximum transport is achieved via an array of square *convection* cells (rolls) with optimal aspect ratio $\Gamma_{\mathrm{opt}} = 1$. Figure 2 shows this flow field where the square convection cells are clearly seen. The computed flow field (equations (43)-(44) and (47)), and the square cells closely resemble those of the flow in porous media at the onset of linear instability (see e.g. [6]). Additionally, the factor $4\pi^2$ arising in (52) is the critical Ra for instability.

2.3 Small to Large Pe: Numerical Solution

The solution in the limit of small Pe was obtained analytically from the linearized equations in the last section. To find the solution for any Pe, especially for large Pe, the full nonlinear equations (26)-(29) must be solved. Taking the curl of (26) and defining the stream function ψ as $(u = \partial\psi/\partial z, w = -\partial\psi/\partial x)$, (26)-(29) reduce to

$$\begin{aligned} \mathrm{J}(\theta, \phi) + \mu\, \Delta\psi + (\theta + \phi)_x &= 0, & (53)\\ -\mathrm{J}(\psi, \phi) + \Delta\phi - \psi_x &= 0, & (54)\\ -\mathrm{J}(\psi, \theta) - \Delta\theta + \psi_x &= 0, & (55) \end{aligned}$$

where $\mathrm{J}(a, b) = \frac{\partial a}{\partial x}\frac{\partial b}{\partial z} - \frac{\partial a}{\partial z}\frac{\partial b}{\partial x}$ is the Jacobian. Boundary conditions (31)-(33) become

$$\begin{aligned} \psi(x, 0) = \psi(x, 1) &= 0, & (56)\\ \theta(x, 0) = \theta(x, 1) &= 0, & (57)\\ \phi(x, 0) = \phi(x, 1) &= 0. & (58) \end{aligned}$$

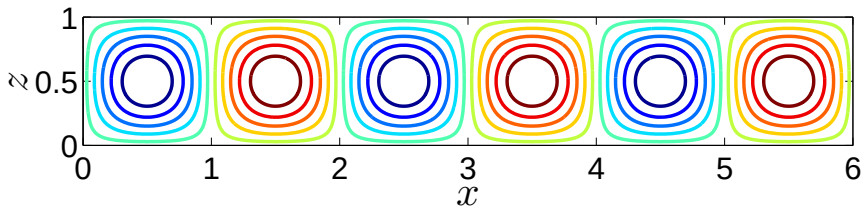

(a)

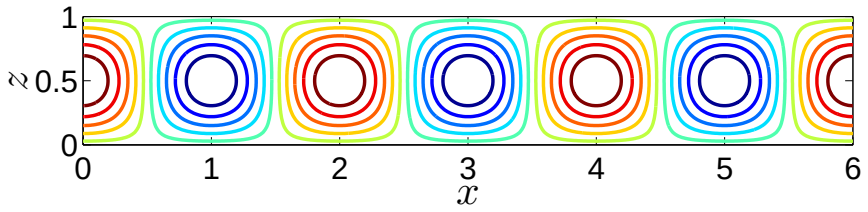

(b)

Figure 2: Optimal flow field in the small Pe limit for the fixed energy problem: (a) streamlines ψ, (b) temperature θ.

The above equations and boundary conditions imply an interesting symmetry between θ and ϕ which will be exposed in the numerical results and exploited later to obtain asymptotic solutions.

Rewritten for ψ, equations (30) and (16) are

$$\mathrm{Pe}^2 = \langle \psi_x^2 + \psi_z^2 \rangle , \tag{59}$$

$$\mathrm{Nu}_{\max} = 1 - \langle \psi_x \theta \rangle . \tag{60}$$

Below we present the numerical solution of these equations, obtained using continuation.

2.3.1 Numerical Continuation

Numerical continuation is a strategy to systematically trace a branch of solutions starting from a first guess [3]. In our problem, for a given Γ, we know the solution (analytically) in the limit of small Pe (i.e. large μ), and we want to find the solutions numerically for larger values of Pe (i.e. smaller μ). The continuation algorithm is:

1. We start from the analytical solution for large μ for a given value of Γ.
2. At iteration $N+1$, μ^{N+1} is set to be $0.1\% - 5\%$ smaller than μ^N. We use the solution at iteration N (with μ^N) as a first guess and iteratively find the solution at iteration $N+1$ (with μ^{N+1}).
3. Using the converged solution of step 2, we calculate $\mathrm{Pe}(\mu^{N+1}, \Gamma)$ and $\mathrm{Nu}_{\max}(\mu^{N+1}, \Gamma)$ from (59) and (60), respectively.
4. Steps 2 and 3 are repeated to reduce μ (i.e. increase Pe) by several orders of magnitude.
5. Steps 1–4 are repeated for several values of Γ.

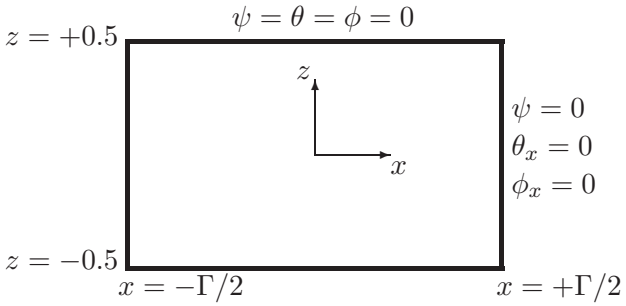

Figure 3: The fixed energy problem: the geometry and boundary conditions of the computational domain corresponding to a single 2D cell. Boundary conditions on the bottom (left) boundary are the same as top (right) boundary.

The result of steps 1–5 is to obtain $\mathrm{Nu}_{\max}(\mathrm{Pe}, \Gamma)$ for a wide range of Pe and Γ. In step 1, the vertical wavenumber m should also be chosen for the linear solution. As discussed later, $\mathrm{Nu}_{\mathrm{MAX}}$ is always obtained with solutions continued from a linear solution with $m = 1$; therefore, for most of the cases we used $m = 1$, although cases with $m = 2$ and linearly superposed solutions with different values of m also have been studied (see section 2.3.3). The percentage reduction of μ in step 2 depends on the degree of nonlinearity of the problem (μ should be varied more slowly as Pe increases). The next section presents details of the iterative method and the numerical scheme used in step 2.

2.3.2 Numerical Method

We use the Newton–Kantorovich iteration scheme [3] with the pseudo–spectral Chebyshev collocation method [18, 3] to solve (53)–(55). Instead of solving these equations in a large horizontally periodic domain including multiple cells (such as the one shown in Figure 2a), we choose the computational domain to be a single cell. Therefore, the computational domain is between the horizontal walls and has a width Γ (Figure 3). This unicellular approach has been used before with great success to study the Rayleigh–Bénard convection [4] and porous media convection [5]. Symmetry boundary conditions have been used on the vertical sides of the domain (at $x = \pm\Gamma/2$). Note that in the computational domain the horizontal walls are located at $z = \pm 0.5$ (instead of $z = 0, 1$ we used before), for convenience when Chebyshev polynomials are employed.

In the following, we describe the Newton–Kantorovich method [3] used in step 2 of the continuation algorithm (section 2.3.1). We use the known solution of the Nth iteration $(\psi^N, \theta^N, \phi^N)$ as a first guess to iteratively find a good approximation of the true solution at the $N + 1$th iteration $(\psi^{N+1}, \theta^{N+1}, \phi^{N+1})$. Rewriting equations (53)-(55) as

$$\Delta\psi = \mathrm{F}(\theta_x, \theta_z, \phi_x, \phi_z) \tag{61}$$

$$\Delta\theta = \mathrm{G}(\psi_x, \psi_z, \theta_x, \theta_z) \tag{62}$$

$$\Delta\phi = \mathrm{Q}(\psi_x, \psi_z, \phi_x, \phi_z) \tag{63}$$

and Taylor expanding the nonlinear terms F, G, and Q about the solution of the Nth iteration gives

$$\Delta\psi^{N+1} = \mathrm{F}^N + \delta\theta_x\,\mathrm{F}^N_{\theta_x} + \delta\theta_z\,\mathrm{F}^N_{\theta_z} + \delta\phi_x\,\mathrm{F}^N_{\phi_x} + \delta\phi_z\,\mathrm{F}^N_{\phi_z} + \text{H.O.T}, \tag{64}$$

$$\Delta\theta^{N+1} = \mathrm{G}^N + \delta\psi_x\,\mathrm{G}^N_{\psi_x} + \delta\psi_z\,\mathrm{G}^N_{\psi_z} + \delta\theta_x\,\mathrm{G}^N_{\theta_x} + \delta\theta_z\,\mathrm{G}^N_{\theta_z} + \text{H.O.T}, \tag{65}$$

$$\Delta\phi^{N+1} = \mathrm{Q}^N + \delta\psi_x\,\mathrm{Q}^N_{\psi_x} + \delta\psi_z\,\mathrm{Q}^N_{\psi_z} + \delta\phi_x\,\mathrm{Q}^N_{\phi_x} + \delta\phi_z\,\mathrm{Q}^N_{\phi_z} + \text{H.O.T}, \tag{66}$$

where the subscripts in F, G, and Q denote the Frechet derivatives (e.g. $F_{\psi_x} \equiv \partial F/\partial\psi_x$) (the superscript N means evaluated at iteration N). δ of any quantity is defined as the difference between its value at iterations $N+1$ and N (e.g. $\delta\psi \equiv \psi^{N+1} - \psi^N$). The neglected higher order terms (H.O.T) are $O((\delta\theta_x)^2, (\delta\theta_z)^2, (\delta\phi_x)^2, (\delta\phi_z)^2)$ or smaller. Following the detailed procedure presented in Appendix A, we obtain a system of three linear differential equations (199)–(201). Applying a pseudo–spectral Chebyshev collocation method in both x and z directions results in the following linear matrix equation:

$$\begin{bmatrix} \mu\Delta & (I+\phi^N_z)D_x - \phi^N_x D_z & (I-\theta^N_z)D_x + \theta^N_x D_z \\ -(I-\theta^N_z)D_x - \theta^N_x D_z & \Delta - \psi^N_z D_x + \psi^N_x D_z & O \\ -(I+\phi^N_z)D_x + \phi^N_x D_z & O & \Delta + \psi^N_z D_x - \psi^N_x D_z \end{bmatrix} \begin{bmatrix} \delta\psi \\ \delta\theta \\ \delta\phi \end{bmatrix} = \begin{bmatrix} -\mu\Delta\psi^N - (I+\phi^N_z)\theta^N_x - (I-\theta^N_z)\phi^N_x \\ -\Delta\theta^N + (I-\theta^N_z)\psi^N_x + \psi^N_z\theta^N_x \\ -\Delta\phi^N + (I+\phi^N_z)\psi^N_x - \psi^N_z\phi^N_x \end{bmatrix} \tag{67}$$

where I and O are $M^2 \times M^2$ identity and zero matrices, respectively (M is the number of collocation grid points.) D_x and D_z are the x and z differentiation matrices, respectively; $\Delta = D_{xx} + D_{zz}$. These matrices (with size $M^2 \times M^2$) are constructed using tensor products (also known as Kronecker products) as described in detail in [18]. Boundary conditions are implemented by modifying the rows corresponding to the boundary grid points in the coefficient matrix and the right–hand side matrix in (67). A MATLAB code was developed to construct the elements of (67) and solve it by direct matrix inversion. Once $\delta\psi$, $\delta\theta$, and $\delta\phi$ are calculated, the solution is updated as $\psi^{N+1} = \psi^N + \delta\psi$, $\theta^{N+1} = \theta^N + \delta\theta$, and $\phi^{N+1} = \phi^N + \delta\phi$. The iterations stop when $\delta(\cdot)/\|(\cdot)\|_\infty \le 10^{-10}$ for all three variables ψ, θ, and ϕ. The Clenshaw-Curtis quadrature [18] is used for all spatial integrations, for example to calculate (59) and (60).

2.3.3 Numerical Results

All the results presented here are obtained using $M = 61$ or 91. The iterative solution always converged in less than 6 iterations, and the converged solution satisfies (53)-(55) with a relative error of 10^{-10} or smaller, except at the boundaries. Note that we did not solve these equations for the boundary grid points, and instead we used the freed rows in (67) to enforce the Dirichlet and Neumann boundary conditions. The converged solution satisfies the vertical and horizontal boundary conditions with an absolute error of 10^{-10} or smaller.

Figure 4 shows ψ and θ for the case with $\Gamma = 1$ for low to high values of Pe. As Pe increases, $\mathrm{Nu}_{\max}$ increases as well. The flow shown in Figures 4a and 4b is still in the linear regime. As Pe (and hence the nonlinearity) increases, the bulk flow structure

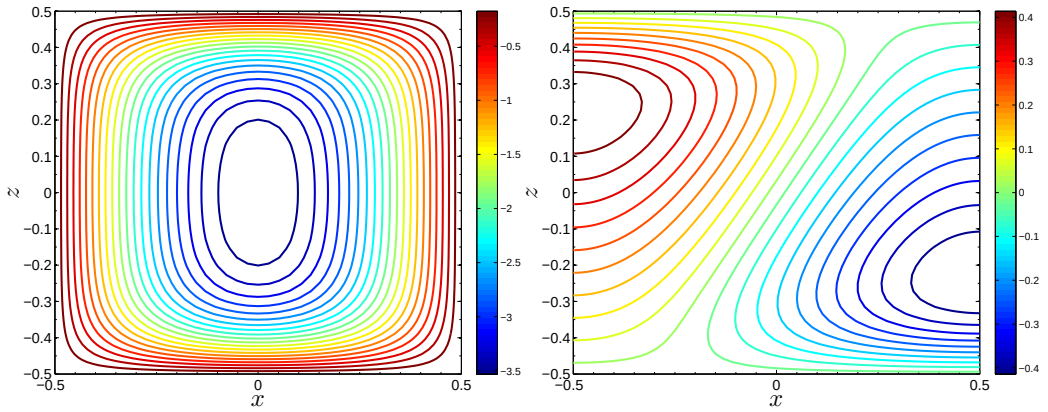

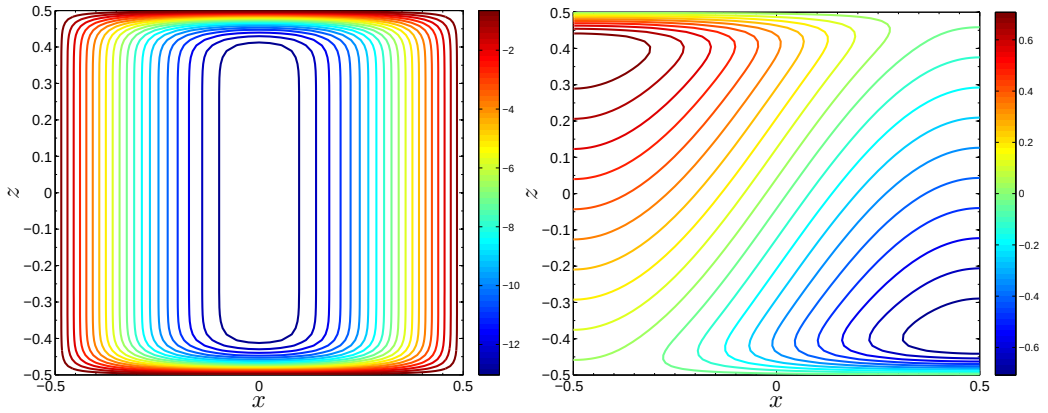

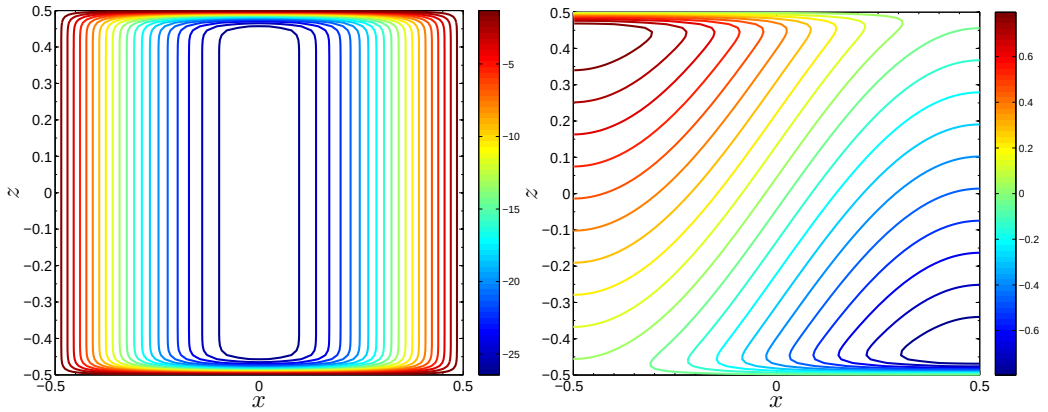

Figure 4: Evolution of the flow fields with Pe for the case with $\Gamma = 1$. Panels on the left show ψ and panels on the right show θ. (a) Pe = 10.0, $\mathrm{Nu}_{\max} = 2.4$, (b) Pe = 59.4, $\mathrm{Nu}_{\max} = 9.7$, (c) Pe = 161.3, $\mathrm{Nu}_{\max} = 20.7$. The resolution is 61^2.

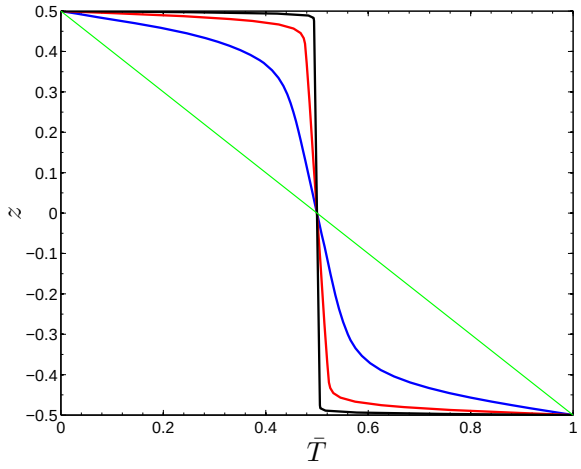

Figure 5: Vertical profiles of the horizontally averaged temperature $\bar{T}(z) = \Theta(z) + 1/\Gamma \int_0^\Gamma \theta(x,z)\mathrm{d}x$ for Pe = 25.6 (blue), Pe = 161.3 (red), and Pe = 1569.9 (black). The thin green line shows $\bar{T} = \Theta$ (i.e. the purely conducting case, Pe = 0). $\Gamma = 1$ and $M = 61$.

changes, and also boundary layers start to develop in both ψ and θ (Figures 4c–4f). The boundary layers become thinner as Pe increases. Figure 5 clearly demonstrates the thinning of the thermal boundary layer by showing the horizontally averaged temperature $\bar{T}(z) = \Theta(z) + 1/\Gamma \int_0^\Gamma \theta(x,z)\mathrm{d}x$ for Pe $= 0, 25.6, 161.3$ and 1569.9. In fact, this decrease in the thermal boundary layer thickness is responsible for the increase of the vertical heat flux (and consequently Nu). This is because the thinner thermal boundary layers have larger temperature gradients (and heat fluxes) at the walls (as seen in Figure 5). Note that at the walls, $\mathbf{q}_\mathrm{a} \cdot \mathbf{z} = -\partial T/\partial z|_{z=0,1}$ because $w = 0$. Additionally, it is easy to show that the horizontally averaged vertical flux does not vary with z, i.e. $\partial\{1/\Gamma \int_0^\Gamma (\mathbf{q}_\mathrm{a}\cdot\mathbf{z})\mathrm{d}x\}/\partial z = 0$ (see e.g. [6]). Therefore, the Nusselt number can be readily calculated using the horizontally averaged vertical flux at one wall, i.e. $\mathrm{Nu} = -1/\Gamma \int_0^\Gamma \{\partial T/\partial z|_{z=0}\}\mathrm{d}x$. An immediate result of this analysis is that $\mathrm{Nu} \propto 1/\delta_T$ where δ_T is the thermal boundary layer thickness.

Figure 6 presents the numerically calculated $\mathrm{Nu}_{\max}(\mathrm{Pe}, \Gamma)$ for several values of Γ. This figure shows that:

- The absolute upper bound (24) overpredicts the maximum possible heat transport.
- $\mathrm{Nu}_{\mathrm{MAX}}(\mathrm{Pe})$ is obtained with solutions continued from linear solutions with $m = 1$. This was expected because flows with $m > 1$ produce horizontal transport in the bulk (far from the walls) which is not desired and wastes the energy of the flow. We computed several cases with $m > 1$ and a few cases with superposed solutions of two m (only one case is shown in this figure) and they all confirmed this conclusion.
- In the limit of small Pe, $\mathrm{Nu}_{\max}$ agrees well with the analytical bound (51).
- as Pe (and therefore nonlinearity) increases, $\mathrm{Nu}_{\max}$ starts to scale as $K(\Gamma)\,\mathrm{Pe}^{2/3}$.
- As Pe increases, $\mathrm{Nu}_{\mathrm{MAX}}$ is obtained for flows with smaller Γ. This figure clearly demonstrate that $\mathrm{Nu}_{\max}$ plotted against Pe for different values of Γ forms an envelope

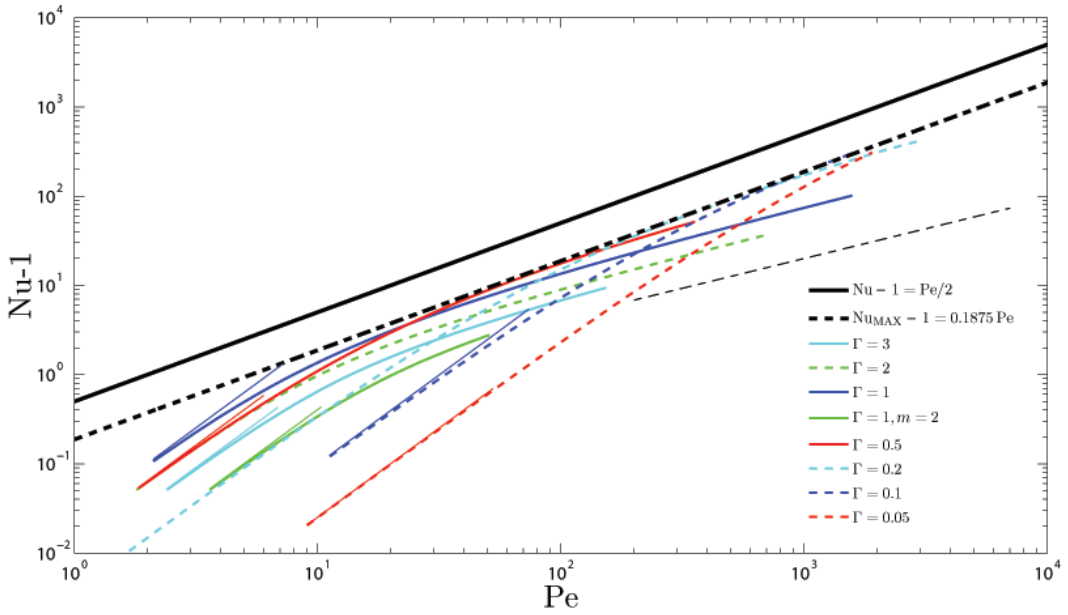

Figure 6: The non-black lines show the numerically obtained $\mathrm{Nu}_{\max}$ as a function of Pe for various values of Γ. For each case, the thin short line of the same color, visible for most of the cases, shows the analytical $\mathrm{Nu}_{\max}$ (51) in the limit of small Pe. The thick solid black line shows the absolute upper bound (24), and the thick broken black line shows the analytically obtained $\mathrm{Nu}_{\mathrm{MAX}}$ (130) (see the next section). The thin broken black line indicates the $\mathrm{Pe}^{2/3}$ slope. All numerical results started with linear solutions with $m = 1$, unless otherwise stated. All results shown here have resolution $M = 61$. Using a higher resolution $M = 91$ results in negligible difference.

which determines $\mathrm{Nu}_{\mathrm{MAX}}$. The numerical results suggests that $\mathrm{Nu}_{\mathrm{MAX}}$ scales as $C\,\mathrm{Pe}$ where C is a constant prefactor.

The prefactors $K(\Gamma)$ and C can be determined from the numerical results. However, this is not necessary as in the next section, guided by the numerical results, we obtain analytical solutions for (53)–(55) and hence $\mathrm{Nu}_{\max}$, $\mathrm{Nu}_{\mathrm{MAX}}$, and Γ_{opt} in the limit of large Pe (the analytically obtained $\mathrm{Nu}_{\mathrm{MAX}}$ is shown in Figure 6 and agrees very well with the envelope produced by the numerical results).

2.4 The Limit of Large Pe: Asymptotic Solution

The numerical results show various symmetries in ψ, θ, and ϕ in the limit of large Pe (e.g. see Figures 7 and 8). ψ is found to be nearly independent of z in the bulk and to depend on x as $\cos(\pi x/\Gamma)$ in both the bulk and boundary layers. θ and ϕ do not have such simple structure in the bulk or boundary layer. However, defining

$$\xi(x,z) \equiv \phi(x,z) + \theta(x,z), \tag{68}$$

$$\eta(x,z) \equiv \theta(x,z) - \phi(x,z), \tag{69}$$

it is observed that ξ (like ψ) is nearly independent of z except close to the top and bottom boundaries (i.e. inside the thin boundary layers), and that η is only a function of z everywhere (see Figures 7 and 8). This simple geometric structure suggests rewriting the equations for (ψ, ξ, η) and using matched asymptotic analysis to solve the resulting equations in the large–Pe (i.e. small–μ) limit.

Rewriting (53)-(55) for ψ, ξ, and η yields

$$\begin{aligned} -\,\mathrm{J}(\xi,\eta) + 2\mu\Delta\psi + 2\xi_x &= 0, && (70)\\ \mathrm{J}(\psi,\xi) + \Delta\eta &= 0, && (71)\\ \mathrm{J}(\psi,\eta) + \Delta\xi - 2\psi_x &= 0, && (72) \end{aligned}$$

where (71) and (72) are obtained from adding and subtracting (54) and (55), respectively.

The numerical results suggest using the following ansatzen:

$$\begin{aligned} \psi &= \bar{\psi}(x)\; A(z), && (73)\\ \xi &= \bar{\xi}(x)\; B(z), && (74)\\ \eta &= \bar{\eta}(z)\; C(z), && (75) \end{aligned}$$

where the overbar indicates the interior solution (or the so-called *outer solution*, i.e. far from the top and bottom boundary layers), and A, B, and C are equal to unity in the interior, rapidly decay close to the boundaries, and vanish at $z = \pm 0.5$. The first step in the analysis is finding the interior solution ($\bar{\psi}$,$\bar{\xi}$,$\bar{\eta}$).

2.4.1 Interior Solution

For small μ, the leading-order dominant balances in (70)–(72) in the interior are

$$\begin{aligned} 2\mu\psi_{xx} - \xi_x\eta_z + \xi_z\eta_x + 2\xi_x &= 0, && (76)\\ \eta_{xx} + \eta_{zz} + \psi_x\xi_z - \psi_z\xi_x &= 0, && (77)\\ \xi_{xx} + \xi_{zz} + \psi_x\eta_z - \psi_z\eta_x - 2\psi_x &= 0, && (78) \end{aligned}$$

where the formally small $2\mu\psi_{xx}$ term has been retained to develop an asymptotic solution that remains uniformly valid in the small-μ limit even as $\Gamma \to 0$ (see below). Motivated by the numerics, we make the ansatz that $\eta(x,z) \sim \bar{\eta}(z)$ and $\psi(x,z) \sim \bar{\psi}(x)$, in the interior, in accord with (73) and (75).

Therefore, (76)–(78) reduce to

$$\begin{aligned} 2\mu\,\bar{\psi}_{xx} + (2 - \bar{\eta}_z)\,\bar{\xi}_x &= 0, && (79)\\ \bar{\eta}_{zz} &= 0, && (80)\\ \bar{\xi}_{xx} + (\bar{\eta}_z - 2)\bar{\psi}_x &= 0. && (81) \end{aligned}$$

Equation (80) shows that $\bar{\eta}$ is linear in z (this could be also inferred from (79) and (81) because $\bar{\psi}$ and $\bar{\xi}$ are only functions of x). The linearity of $\bar{\eta}(z)$ along with the symmetry of the flow with respect to $z = 0$ yields

$$\bar{\eta}(z) = \bar{\eta}_o\, z, \qquad (82)$$

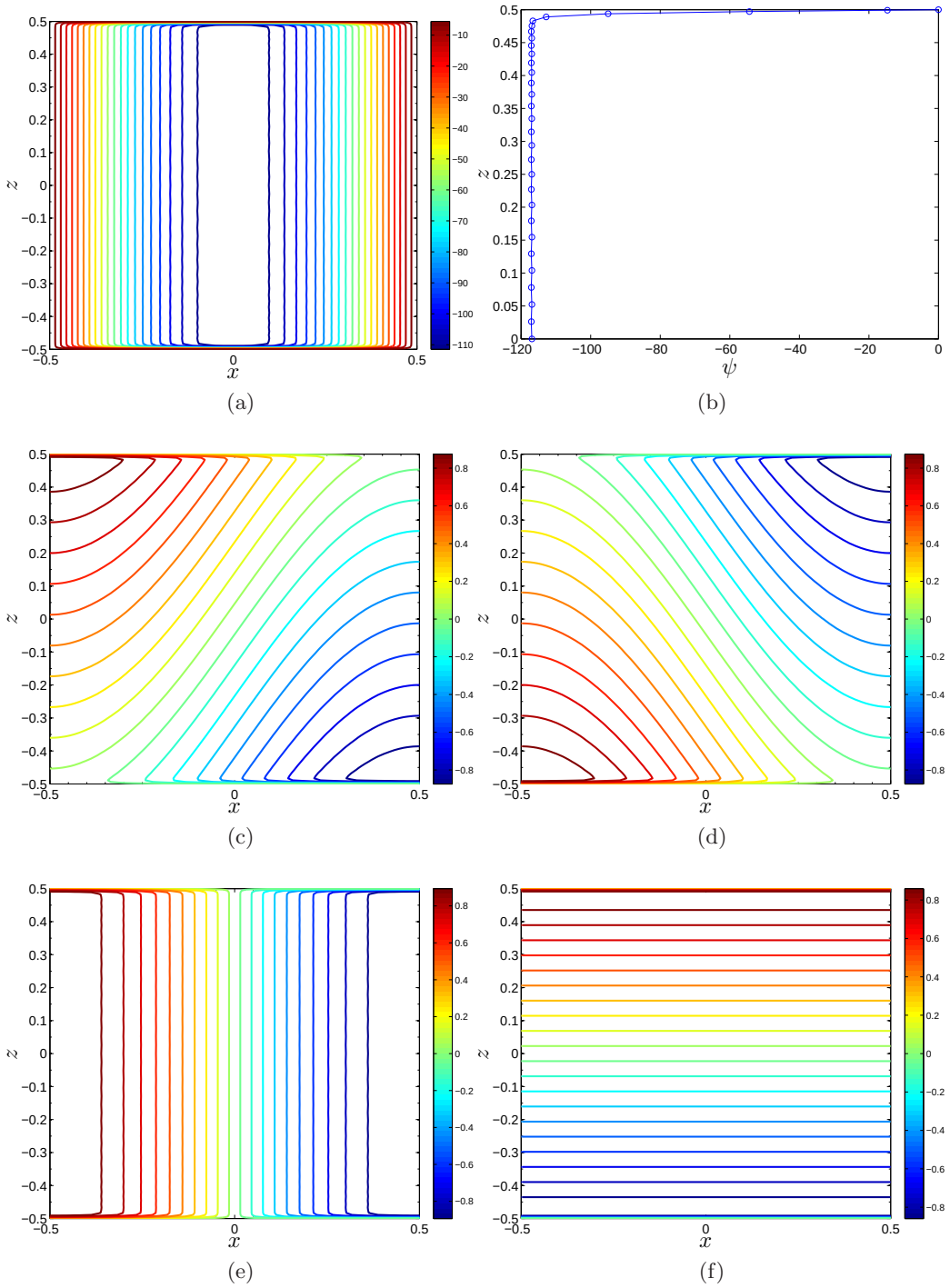

Figure 7: Flow field for $\Gamma = 1$, $\mu = 3.557 \times 10^{-5}$, $\mathrm{Pe} = 1320.5$, and $\mathrm{Nu}_{\max} = 90.7$. (a) ψ, (b) ψ along $x = 0$, (c) θ, (d) ϕ, (e) $\xi \equiv \theta + \phi$, and (f) $\eta \equiv \theta - \phi$. The resolution is 61^2.

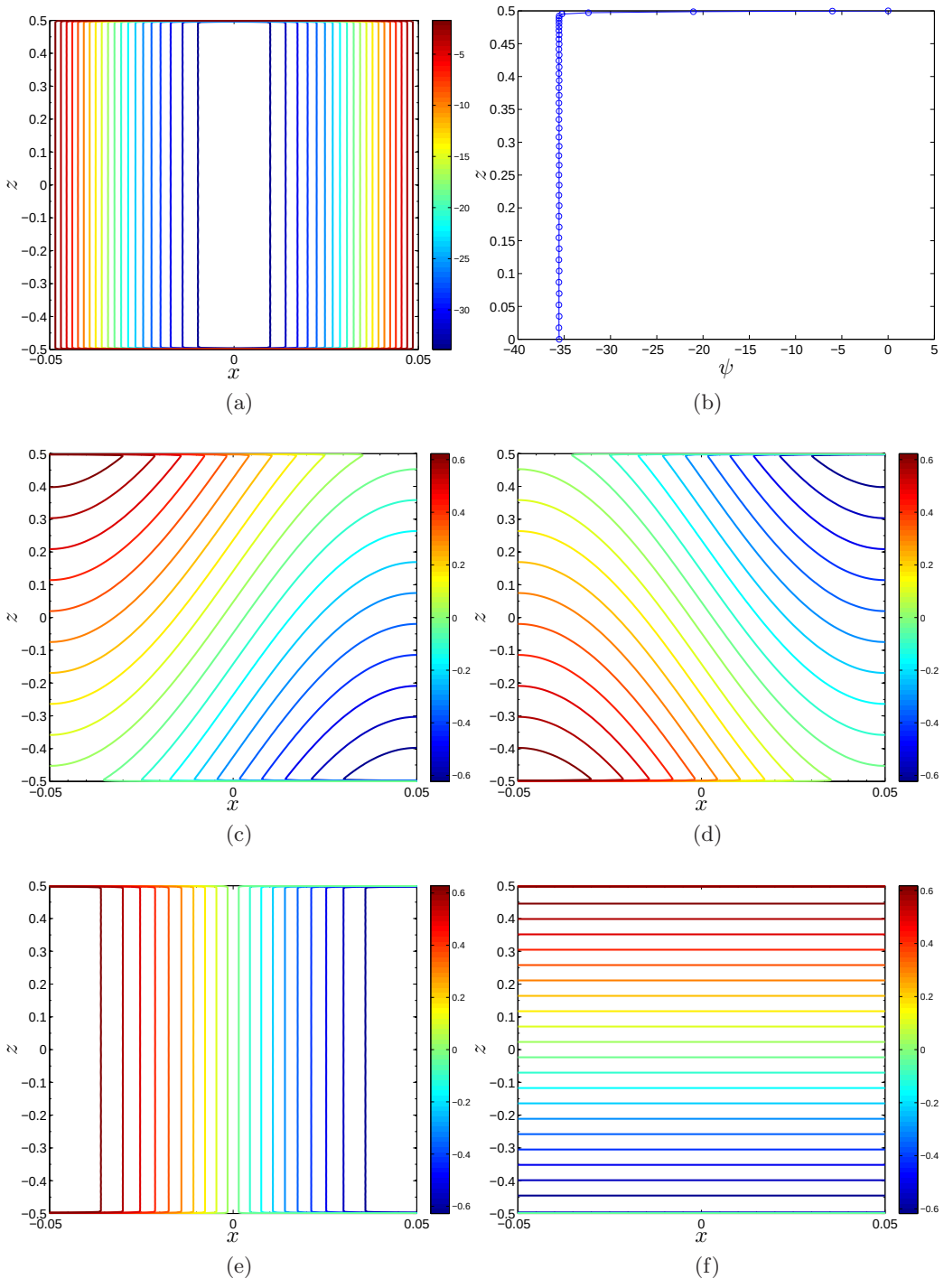

Figure 8: Flow field for $\Gamma = 0.1$, $\mu = 1.9 \times 10^{-4}$, $\mathrm{Pe} = 1045.0$, and $\mathrm{Nu}_{\max} = 194.0$. (a) ψ, (b) ψ along $x = 0$, (c) θ, (d) ϕ, (e) $\xi \equiv \theta + \phi$, and (f) $\eta \equiv \theta - \phi$. The resolution is 91^2.

where $\bar{\eta}_o$ is an unknown constant. Linearity of $\bar{\eta}(z)$ can also be clearly seen from Figures 7f and 8f. Using (82) and eliminating $\bar{\psi}$ between (79) and (81) gives

$$\bar{\xi}_{xxx} + \left(\frac{\bar{\eta}_o - 2}{\sqrt{2\mu}}\right)^2 \bar{\xi}_x = 0. \tag{83}$$

Given the periodicity of 2Γ in x, and $\xi_x(\pm\Gamma/2, z) = 0$, this implies

$$\bar{\xi} = \pm\bar{\xi}_o \sin(\pi\, x/\Gamma), \tag{84}$$

$$\bar{\eta}_o = 2 - \frac{\pi}{\Gamma}\sqrt{2\mu}, \tag{85}$$

where $\bar{\xi}_o > 0$ is an unknown constant. Notice that there exists another possible solution $\bar{\eta}_o = 2 + (\pi/\Gamma)\sqrt{2\mu} > 2$ which is discarded here based on the numerical results. It will be shown later in section 2.4.3 that $\bar{\eta}_o$ must be ≤ 2 because of the maximum principle, confirming that (85) is the only admissible solution.

Equation (81) gives

$$\bar{\psi} = \frac{\pm\bar{\xi}_o}{\sqrt{2\mu}} \cos(\pi\, x/\Gamma). \tag{86}$$

Therefore, the interior flow field (i.e. outer solution) is known up to an unknown constant $\bar{\xi}_o$ (notice that in (84) and (86) either $-\bar{\xi}_o$ or $+\bar{\xi}_o$ should be chosen for both $\bar{\psi}$ and $\bar{\xi}$).

2.4.2 Boundary Layer Solution

To find the boundary layer solution (i.e. the inner solution), we rewrite (73)-(75) as

$$\psi = \bar{\psi}(x)\, A(Z_1), \tag{87}$$

$$\xi = \bar{\xi}(x)\, B(Z_2), \tag{88}$$

$$\eta = \bar{\eta}(z)\, C(Z_3), \tag{89}$$

where Z is the rescaled z near the boundaries at $z = \mp 0.5$:

$$Z_1 = (0.5 \pm z)/\delta_1, \tag{90}$$

$$Z_2 = (0.5 \pm z)/\delta_2, \tag{91}$$

$$Z_3 = (0.5 \pm z)/\delta_3. \tag{92}$$

For the moment we allow for the possibility that the small boundary layer thicknesses for ψ, ξ, and η are not the same. Notice that in the rescaled coordinate, $A(0) = B(0) = C(0) = 0$ and $A(+\infty) = B(+\infty) = C(+\infty) = 1$.

Focusing only on the upper boundary layer for now (i.e. close to $z = +0.5$), and using (87)-(89) and (90)-(92) in (70)-(72) gives

$$2\mu\,(\bar{\psi}_{xx}\, A + \bar{\psi}\, A''/\delta_1^2) + (2 - (\bar{\eta}_z\, C - \bar{\eta}\, C'/\delta_3))\,\bar{\xi}_x\, B = 0, \tag{93}$$

$$\bar{\eta}_{zz}\, C - 2\bar{\eta}_z\, C'/\delta_3 + \bar{\eta}\, C''/\delta_3^2 - \bar{\psi}_x\, A\,\bar{\xi}\, B'/\delta_2 + \bar{\xi}_x\, B\,\bar{\psi}\, A'/\delta_1 = 0, \tag{94}$$

$$\bar{\xi}_{xx}\, B + \bar{\xi}\, B''/\delta_2^2 - (2 - (\bar{\eta}_z\, C - \bar{\eta}\, C'/\delta_3))\bar{\psi}_x\, A = 0, \tag{95}$$

where $'$ means d/dZ (e.g. $A' \equiv dA/dZ_1$). Using the interior solution (82)-(86), and noticing that $\bar{\eta} \to \bar{\eta}_o/2$ as $z \to 0.5$, the above equations yield

$$\sqrt{2\mu}\left[-\left(\frac{\pi}{\Gamma}\right)^2 A + \frac{1}{\delta_1^2}A''\right] + \left(\frac{\pi}{\Gamma}\right)\left[2 - \left(2 - \frac{\pi}{\Gamma}\sqrt{2\mu}\right)\left(C - \frac{1}{2\delta_3}C'\right)\right] B = 0, \quad (96)$$

$$\left(2 - \frac{\pi}{\Gamma}\sqrt{2\mu}\right)\left[-\frac{2}{\delta_3}C' + \frac{1}{2\delta_3^2}C''\right] + \left(\frac{\pi}{2\Gamma}\right)\frac{\bar{\xi}_o^2}{\sqrt{2\mu}}\left[\frac{1}{\delta_2}AB' + \frac{1}{\delta_1}BA'\right] = 0, \quad (97)$$

$$\sqrt{2\mu}\left[-\left(\frac{\pi}{\Gamma}\right)^2 B + \frac{1}{\delta_2^2}B''\right] + \left(\frac{\pi}{\Gamma}\right)\left[2 - \left(2 - \frac{\pi}{\Gamma}\sqrt{2\mu}\right)\left(C - \frac{1}{2\delta_3}C'\right)\right] A = 0, \quad (98)$$

where (97) has been integrated over $1/\Gamma \int_0^\Gamma \mathrm{d}x$ to eliminate the $\sin^2(\pi x/\Gamma)$ and $\cos^2(\pi x/\Gamma)$ terms.

To balance the leading order terms, we need to determine the generic boundary layer thickness δ as a function of a small parameter ϵ defined based on μ and Γ. To get to the large Pe limit, we know that $\mu \ll 1$, although from the above equations it seems that $\sqrt{\mu} \ll 1$ is a more appropriate parameter in this problem. Here we restrict our analysis to $\Gamma \leq 1$, because the numerical results of section 2.3 showed that $\Gamma > 1$ does not maximize the transport. With $\mu \ll 1$ and $\Gamma \leq 1$, we define $\lambda \equiv \Gamma\sqrt{\mu} \ll 1$. We also need to consider the magnitude of $\sigma \equiv \Gamma/\sqrt{\mu}$. If $\Gamma = \mathcal{O}(1)$, then $\sigma \gg 1$. The numerical results (Figure 6) suggest that Γ_{opt} decreases as Pe increases. Therefore, we should allow for the possibility that $\Gamma \ll 1$, i.e. $\sigma = \mathcal{O}(1)$ and $\sigma \ll 1$. However, the latter means that the cell size shrinks very fast as Pe increases, suggesting that this limit probably does not correspond to the optimal flow. A close examination of (96)-(98) reveals that $\sigma \gg 1$ and $\sigma = \mathcal{O}(1)$ give the same balance and result in the same scaling for boundary layer thicknesses. Therefore one solution covers both limits. Additionally, the distinguished limit $\sigma = \mathcal{O}(1)$ guarantees that the solution is uniformly valid in Γ. Here we focus on these two limits and exclude $\sigma \ll 1$ from our analysis (but appendix B includes a brief discussion of the scaling in this limit). Therefore, based on the above discussion, we choose the small parameter ϵ as

$$\epsilon \equiv \frac{\Gamma\sqrt{2\mu}}{\pi} \quad (99)$$

where the constants are included to simplify the algebra. Again we emphasize that we only focus on $\sigma \geq \mathcal{O}(1)$ hereafter. This will be justified later as we show that $\text{Nu}_{\max}$ for a fixed value of Γ in the limit of large Pe is obtained with $\sigma \gg 1$, and that Nu_{MAX} for large Pe is achieved when $\sigma = \mathcal{O}(1)$.

Using (99) in (96)-(98), and balancing the leading order terms gives

$$A'' + \left(1 - \frac{\pi}{\sigma\sqrt{2}}\right) B\, C' = 0, \quad (100)$$

$$\epsilon\, \delta_3 = \delta_1^2. \quad (101)$$

Notice that based on our assumption for σ, the term in the parentheses is $\mathcal{O}(1)$. The same procedure for (98) results in

$$B'' + \left(1 - \frac{\pi}{\sigma\sqrt{2}}\right) A\, C' = 0, \quad (102)$$

$$\epsilon\, \delta_3 = \delta_2^2, \quad (103)$$

showing that $\delta_1 = \delta_2 \equiv \delta$. Equation (97) yields

$$\left(1 - \frac{\pi}{\sigma\sqrt{2}}\right) C'' + \frac{\bar{\xi}_o^2}{2}\left(AB' + BA'\right) = 0, \tag{104}$$

$$\epsilon\,\delta = \delta_3^2. \tag{105}$$

Equations (101), (103), and (105) together show that the boundary layer thicknesses are each $\mathcal{O}(\epsilon)$, i.e. $\delta_1 = \delta_2 = \delta_3 = \delta = \epsilon$. Integrating equation (104) gives

$$\left(1 - \frac{\pi}{\sigma\sqrt{2}}\right) C' = -\frac{\bar{\xi}_o^2}{2}\left(AB - 1\right), \tag{106}$$

where the constant of integration has been deduced from $C'(+\infty) = 0$ and $A(+\infty) = B(+\infty) = 1$. Substituting this equation in (100) and (102) results in the exactly the same equation for A and B, which along with the fact that they have the same boundary conditions suggests that $A = B$. Using $A = B$ in both equations (100) and (104) shows that $A = B = \left(1 - \pi/(\sigma\sqrt{2})\right) C/\bar{\xi}_o$. Boundary conditions $A(+\infty) = C(+\infty) = 1$ imply that $\bar{\xi}_o = 1 - \pi/(\sigma\sqrt{2})$. Therefore

$$A = B = C, \tag{107}$$

$$A'' + \bar{\xi}_o\, AA' = 0, \tag{108}$$

$$\bar{\xi}_o = \frac{\bar{\eta}_o}{2} = 1 - \frac{\pi}{2\Gamma}\sqrt{2\mu}. \tag{109}$$

Determining $\bar{\xi}_o$ completes the interior solution.

Equation (108) can be integrated once to give

$$A' + \frac{\bar{\xi}_o}{2}A^2 = \frac{\bar{\xi}_o}{2}, \tag{110}$$

where again the constant of integration comes from $A'(+\infty) = 0$ and $A(+\infty) = 1$. Equation (110) is a Riccati equation with the solution

$$A(Z) = \frac{1 - \exp(-\bar{\xi}_o Z)}{1 + \exp(-\bar{\xi}_o Z)} = \tanh\left[\frac{\bar{\xi}_o}{2} Z\right]. \tag{111}$$

2.4.3 The Complete Solution: Matching

We have found the solution for the flow field to leading order, assuming that $\Gamma\sqrt{\mu} \ll 1$ and $\Gamma/\sqrt{\mu}$ is finite or large. Including the bottom boundary layer, and matching the three regions (the interior and the two boundary layers), the complete solution is

$$\psi(x,z) = \frac{1}{\sqrt{2\mu}}\left(1 - \frac{\pi}{2\Gamma}\sqrt{2\mu}\right)\cos\left(\frac{\pi}{\Gamma}x\right) H(z), \tag{112}$$

$$\xi(x,z) = \left(1 - \frac{\pi}{2\Gamma}\sqrt{2\mu}\right)\sin\left(\frac{\pi}{\Gamma}x\right) H(z), \tag{113}$$

$$\eta(x,z) = 2\left(1 - \frac{\pi}{2\Gamma}\sqrt{2\mu}\right) z\, H(z), \tag{114}$$

where

$$\begin{aligned} H(z) &= A\left(\frac{0.5-z}{\delta}\right) A\left(\frac{0.5+z}{\delta}\right) \\ &= \tanh\left[\frac{\pi}{2}\left(1-\frac{\pi}{2\Gamma}\sqrt{2\mu}\right)\frac{z+0.5}{\Gamma\sqrt{2\mu}}\right]\tanh\left[\frac{\pi}{2}\left(1-\frac{\pi}{2\Gamma}\sqrt{2\mu}\right)\frac{z+0.5}{\Gamma\sqrt{2\mu}}\right]. \end{aligned} \quad (115)$$

Therefore

$$u(x,z) = \frac{1}{\sqrt{2\mu}}\left(1-\frac{\pi}{2\Gamma}\sqrt{2\mu}\right)\cos\left(\frac{\pi}{\Gamma}x\right)H'(z), \quad (116)$$

$$w(x,z) = \frac{1}{\sqrt{2\mu}}\left(\frac{\pi}{\Gamma}\right)\left(1-\frac{\pi}{2\Gamma}\sqrt{2\mu}\right)\sin\left(\frac{\pi}{\Gamma}x\right)H(z), \quad (117)$$

$$\theta(x,z) = \frac{1}{2}\left(1-\frac{\pi}{2\Gamma}\sqrt{2\mu}\right)\left(\sin\left(\frac{\pi}{\Gamma}x\right)+2z\right)H(z). \quad (118)$$

This solution is compared with the numerical results in Figures 9 and 10. The agreement between the numerical and asymptotic solutions is excellent.

Note that the maximum principle requires $|\theta| \le 1$. This means that in (118), the first term in the parentheses, i.e. $\bar{\xi}_o = \bar{\eta}_o/2 = 1-\frac{\pi}{2\Gamma}\sqrt{2\mu}$, has to be smaller than 1. This analysis justifies discarding the other solution for $\bar{\eta}_o$ in section 2.4.1.

Values of Pe and $\mathrm{Nu}_{\max}$ can be calculated analytically from (116)-(118):

$$\mathrm{Pe} = \sqrt{\langle u^2+w^2\rangle} = \frac{1}{2\sqrt{\mu}}\left(1-\frac{\pi}{2\Gamma}\sqrt{2\mu}\right)\sqrt{\int_{-0.5}^{0.5}\{(H')^2+(\pi/\Gamma)^2H^2\}\,\mathrm{d}z} \quad (119)$$

$$\mathrm{Nu}_{\max} = 1+\langle w\theta\rangle = 1+\frac{1}{4\sqrt{2\mu}}\left(\frac{\pi}{\Gamma}\right)\left(1-\frac{\pi}{2\Gamma}\sqrt{2\mu}\right)^2\int_{-0.5}^{0.5}H^2\mathrm{d}z \quad (120)$$

Notice that $H(z)$ depends on μ and Γ which makes it hard to find an explicit expression for $\mathrm{Nu}_{\max}(\mathrm{Pe},\Gamma)$. However, (119) and (120) can be easily calculated numerically for a given pair of (μ,Γ). Figure 11 compares the values of Pe and $\mathrm{Nu}_{\max}$ from the numerical solutions with the values given by (119) and (120) for $\Gamma = 0.2$ and 1. The numerical and analytical results agree well, even for relatively small values of Pe. This suggests that the higher order terms in the analytical solution may be transcendentally small in ϵ.

2.4.4 $\mathrm{Nu}_{\max}(\mathrm{Pe},\Gamma)$: $\lambda \ll 1$ and $\sigma \gg 1$ Limit

In the limit of relatively small $\lambda \equiv \Gamma\sqrt{\mu}$, the integrals in (119) and (120) can be approximated as

$$\int_{-0.5}^{0.5}H^2\mathrm{d}z \approx 1-\frac{4\sqrt{2}}{\pi}\frac{\lambda}{1-\frac{\pi}{\sigma\sqrt{2}}}, \quad (121)$$

$$\int_{-0.5}^{0.5}(H')^2\mathrm{d}z \approx \frac{\sqrt{2}\pi}{3}\frac{1-\frac{\pi}{\sigma\sqrt{2}}}{\lambda}, \quad (122)$$

as has been confirmed numerically (again, recall that $\sigma \equiv \Gamma/\sqrt{\mu}$ is not $\ll 1$).

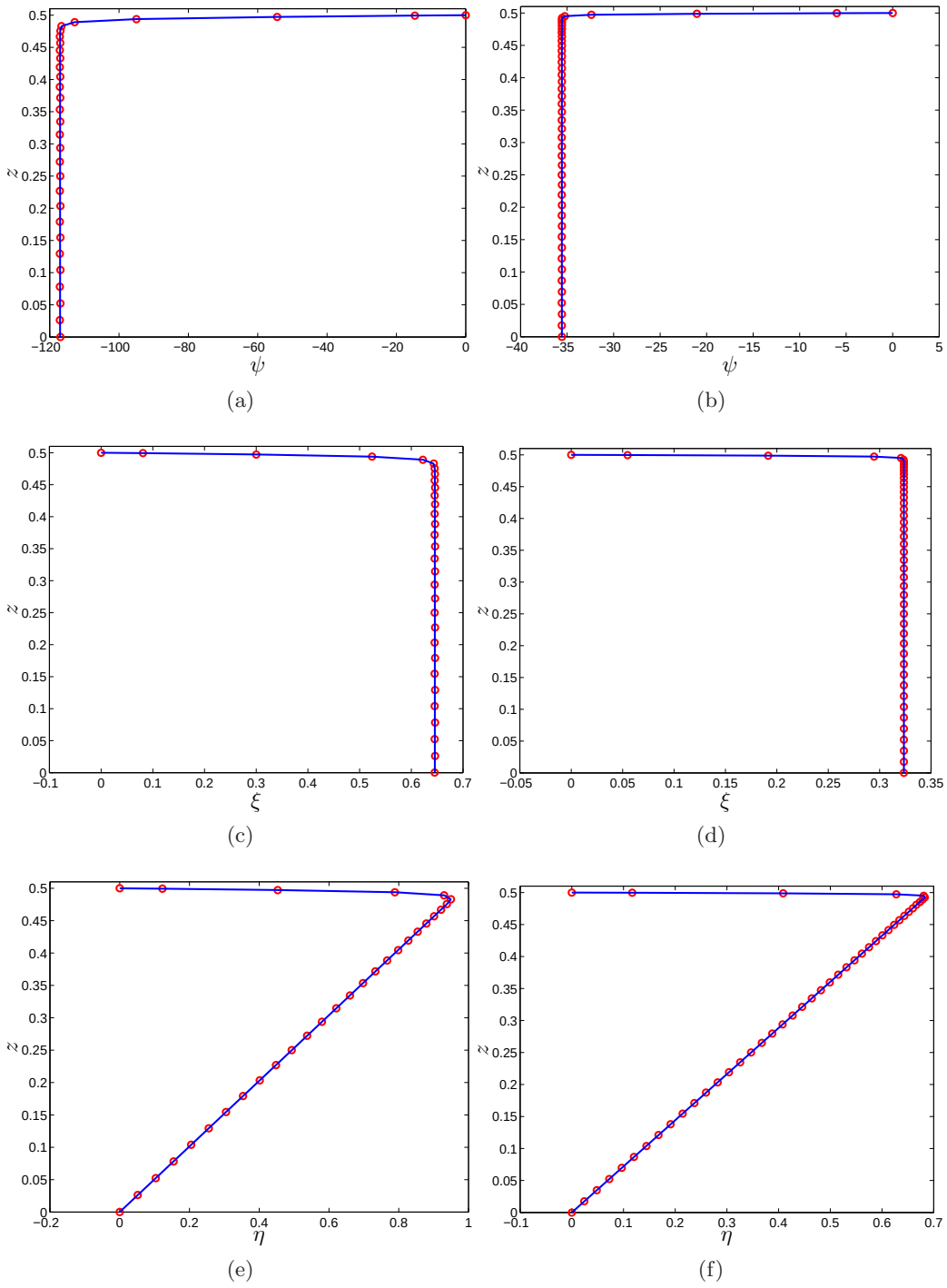

Figure 9: Comparison of the analytical (blue line) and numerical (red circles) solutions for $\Gamma = 1$ (left panels), and $\Gamma = 0.1$ (right panels). The top row is ψ along $x = 0$, the middle row is ξ along $x = -0.227$ (left) and $x = -0.0155$ (right), and the bottom row is η along $x = 0$. For $\Gamma = 1$, $\mathrm{Pe} = 1320.5$, $\mathrm{Nu}_{\max} = 90.7$, and $M = 61$. For $\Gamma = 0.1$, $\mathrm{Pe} = 1045.4$, $\mathrm{Nu}_{\max} = 194.0$, and $M = 91$.

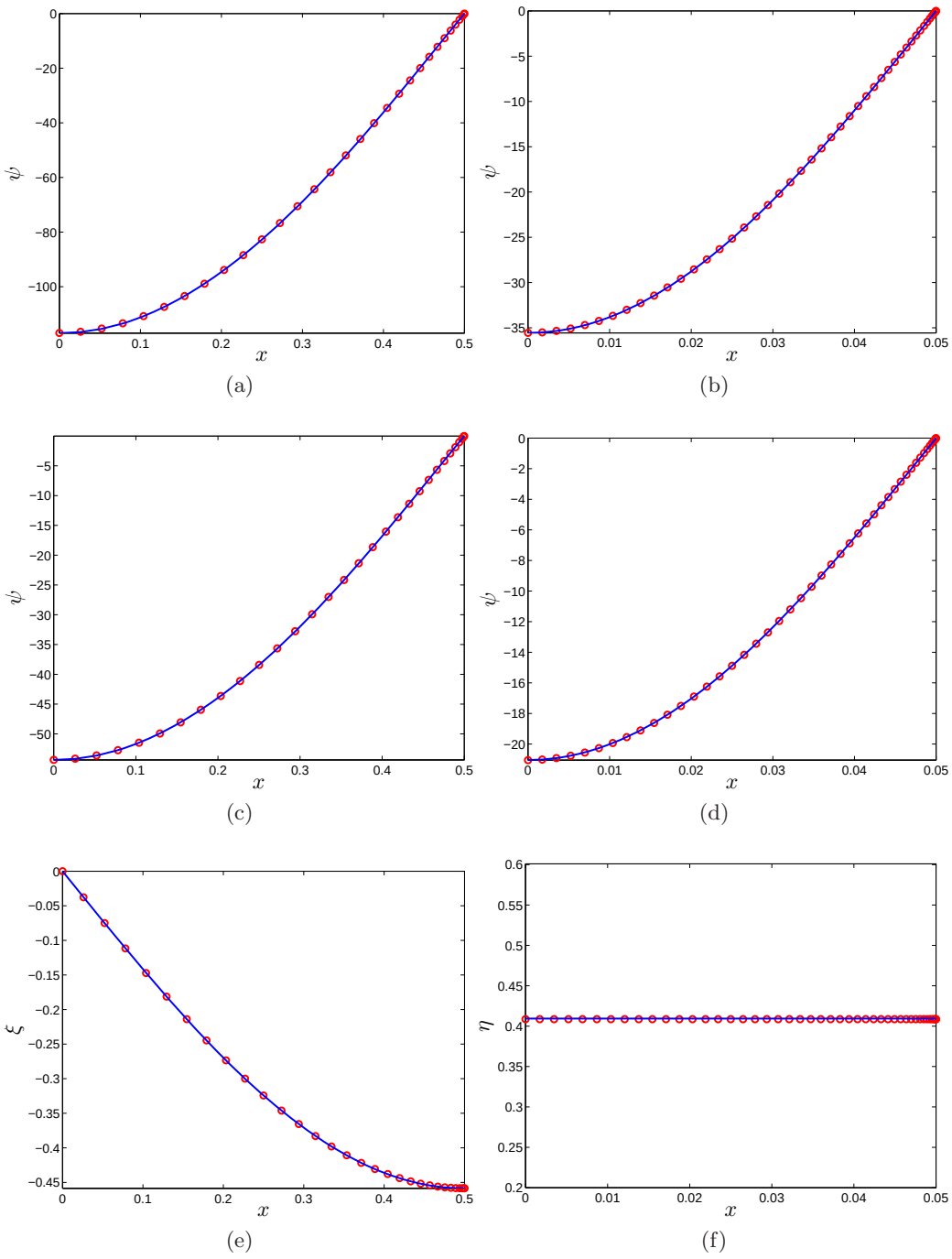

Figure 10: Comparison of the analytical (blue line) and numerical (red circles) solutions for $\Gamma = 1$ (left panels) and $\Gamma = 0.1$ (right panels) (see the caption of Figure 9 for more details). (a) and (b) ψ along $z = 0$. (c) ψ, (d) ψ, (e) ξ, and (f) η; (c)–(f) are versus x along the third Chebyshev collocation point from the wall ($z = 0.4972$ in (c) and $z = 0.4988$ in (d)).

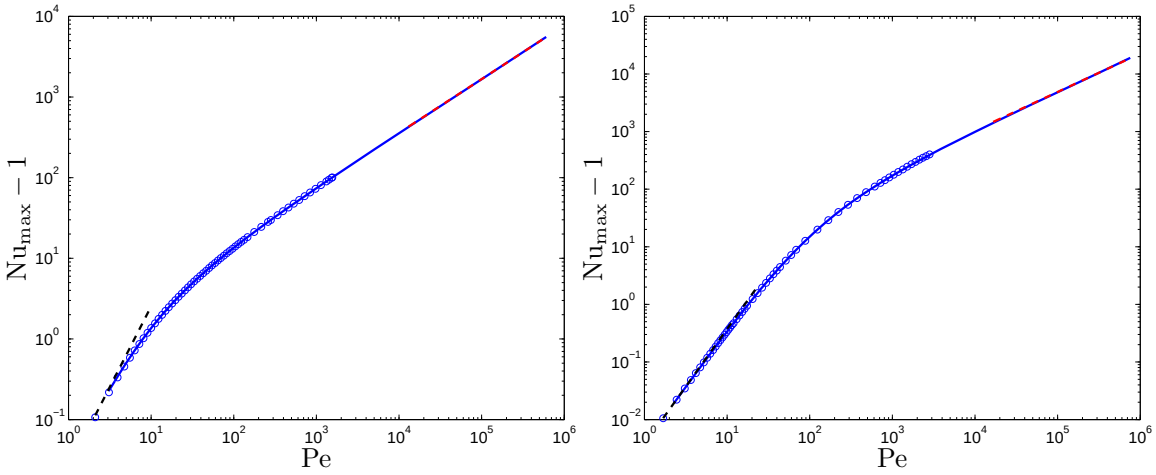

Figure 11: $\mathrm{Nu}_{\max}$ from the numerical solutions (blue circles), the small–Pe analytical solution (51) (dashed black lines), and the large–Pe asymptotic solution (119)-(120) (blue solid lines) for two cases: (a) $\Gamma = 1$ and (b) $\Gamma = 0.2$. The dashed red lines, which have collapsed with the blue lines in the large–Pe regime, show (125).

Here examine (119) and (120) in the limit of vanishing μ and fixed Γ, i.e. $\lambda \ll 1$ and $\sigma \gg 1$. In this limit, (121) and (122) further simplify to 1 and $\sqrt{2}\pi/(3\lambda)$, respectively. Using these limits in (119) and (120) yields

$$\mathrm{Pe} = \frac{\pi}{2}\frac{1}{\lambda}\sqrt{\frac{\sqrt{2}}{3\pi}\sigma}, \tag{123}$$

$$\mathrm{Nu}_{\max} - 1 = \frac{\pi}{4\sqrt{2}}\frac{1}{\lambda}. \tag{124}$$

Solving (123) for μ and using that expression in (124) gives $\mathrm{Nu}_{\max}(\mathrm{Pe}, \Gamma)$:

$$\mathrm{Nu}_{\max} = 1 + \frac{1}{4}\left[\frac{3\pi^2}{\Gamma^2}\right]^{1/3} \mathrm{Pe}^{2/3}. \tag{125}$$

The accuracy of this approximation is shown in Figure 11 for $\Gamma = 0.2$ and 1.

Equation (125) gives $\mathrm{Nu}_{\max}$ as a function of Pe for a fixed value of Γ, which may not be the same as $\mathrm{Nu}_{\mathrm{MAX}}$, i.e. the maximum achievable $\mathrm{Nu}_{\max}$ at that Pe. $\mathrm{Nu}_{\mathrm{MAX}}(\mathrm{Pe})$ is found in the next section and requires letting Γ shrink as Pe increases.

2.4.5 $\mathrm{Nu}_{\mathrm{MAX}}(\mathrm{Pe})$: $\lambda \ll 1$ and $\sigma = \mathcal{O}(1)$ Limit

Here we look at the limit $\sqrt{\mu} \ll 1$ and $\Gamma \ll 1$ when their ratio is finite. Physically this means that as Pe gets larger, we allow the cells to narrow. It turns out that it is in this distinguished limit that $\mathrm{Nu}_{\mathrm{MAX}}$ for a given Pe, i.e. the optimal transport for a given amount of energy, is achieved.

In this limit, (121) again reduces to 1, but (122) cannot be further simplified. Using these approximations for the integrals in (119)–(120) gives

$$\mathrm{Pe} = \frac{\pi}{2}\frac{1}{\lambda}\left(1-\frac{\pi}{\sqrt{2}}\frac{1}{\sigma}\right)\sqrt{\frac{2}{3}+\frac{\sqrt{2}}{3\pi}\sigma}, \tag{126}$$

$$\mathrm{Nu}_{\max}-1 = \frac{\pi}{4\sqrt{2}}\frac{1}{\lambda}\left(1-\frac{\pi}{\sqrt{2}}\frac{1}{\sigma}\right)^2. \tag{127}$$

By dividing (127) by (126) we eliminate λ:

$$\frac{\mathrm{Nu}_{\max}-1}{\mathrm{Pe}} = \frac{1}{2\sqrt{2}}\frac{1-\frac{\pi}{\sqrt{2}}\frac{1}{\sigma}}{\sqrt{\frac{2}{3}+\frac{\sqrt{2}}{3\pi}\sigma}}. \tag{128}$$

Thus we have obtained $\mathrm{Nu}_{\max}(\mathrm{Pe},\sigma)$, which is found to be maximized at

$$\sigma_{\mathrm{opt}} \equiv \frac{\Gamma_{\mathrm{opt}}}{\sqrt{\mu}} = 2\sqrt{2}\pi \approx 8.885766. \tag{129}$$

This gives the aspect ratio Γ_{opt} that maximizes $\mathrm{Nu}_{\max}$ at a given μ. Using $\sigma=\sigma_{\mathrm{opt}}$ in (128) gives $\mathrm{Nu}_{\mathrm{MAX}}(\mathrm{Pe})$:

$$\mathrm{Nu}_{\mathrm{MAX}} = 1+0.1875\,\mathrm{Pe}. \tag{130}$$

Figure 6 shows that (130) gives the maximum possible transport with remarkable accuracy.

Combining (129) and (126) gives $\Gamma_{\mathrm{opt}}(\mathrm{Pe})$, i.e. the optimal cell aspect ratio at a given Pe:

$$\Gamma_{\mathrm{opt}} = 3.8476\ \mathrm{Pe}^{-1/2} \tag{131}$$

Therefore as the Pe number increases, thinner cells provide the maximum transport.

2.5 Example: Application to Porous Media Convection

Here we show that convection in porous media is an example of transport with fixed energy. We find $\mathrm{Nu}_{\max}$ and $\mathrm{Nu}_{\mathrm{MAX}}$ as a function of the Rayleigh number Ra and compare them with the results of previous analytical and numerical investigations.

Convection in a layer of fluid-saturated porous medium heated from below and cooled from above is often modeled by [6]

$$\nabla\cdot\mathbf{v} = 0, \tag{132}$$

$$\frac{1}{\mathrm{Pr}}\left(\dot{\mathbf{v}}+\mathbf{v}\cdot\nabla\mathbf{v}\right)+\mathbf{v} = -\nabla p+\mathrm{Ra}\,T\mathbf{z}, \tag{133}$$

$$\dot{T}+\mathbf{v}\cdot\nabla T = \Delta T, \tag{134}$$

where the first and the third equations are the incompressibility constraint and advection–diffusion equation. The second equation is the Boussinesq momentum equation where Pr is

the Prandtl–Darcy number, and Ra is the Rayleigh number. The linear velocity damping term comes from the Darcy's law (see [6] and references therein for details).

Multiplying (133) by $\mathbf{v}$ and integrating over long time and over the domain with impermeable walls gives

$$\langle \mathbf{v} \cdot \mathbf{v} \rangle = \mathrm{Ra} \, \langle wT \rangle \,, \tag{135}$$

where the transient term vanishes due to long–time averaging, and the nonlinear and pressure terms vanish because of the spatial integration. Using the definition of Pe for fixed energy problems (13) and Nu (16) from section 1.1 we obtain

$$\mathrm{Pe}^2 = \mathrm{Ra} \, (\mathrm{Nu} - 1). \tag{136}$$

The Nusselt number Nu, when calculated by long–time averaging, is just a function of Ra. As a results, in both steady and statistically–steady flows, equation (136) shows that Pe is fixed for a fixed value of Ra (note that Ra depends on the fluid properties and the imposed temperature difference between the walls; it does not depend on the flow). Therefore, convection in porous media occurs with fixed energy.

Employing (136), Pe can be replaced with Ra in (125), (130), and (131):

$$\mathrm{Nu}_{\max}(\mathrm{Ra}, \Gamma) = 1 + \frac{\sqrt{3}\pi}{8\Gamma} \, \mathrm{Ra}^{1/2}, \tag{137}$$

$$\mathrm{Nu}_{\mathrm{MAX}}(\mathrm{Ra}) = 1 + 0.0352 \, \mathrm{Ra}, \tag{138}$$

$$\Gamma_{\mathrm{opt}} = 8.89 \, \mathrm{Ra}^{-0.5}. \tag{139}$$

Interestingly, $\mathrm{Ra}^{-0.5}$ is the scaling of the smallest unstable mode in porous media convection (obtained from linear stability analysis).

Table 1 compares (137)–(139) with the results obtained using other methods in the literature. The classical argument of Malkus [14] and Howard [11], which is based on the marginal stability of the boundary layer, gives $\mathrm{Nu} \sim \mathrm{Ra}$ for convection in porous media [10]. The background method also gives upper bounds on Nu which scale linearly with Ra. The prefactors in the upper bounds have been improved over the years [6, 16, 19].

While we solved (132) and the steady version of (134) for one cell in the current work, we did not solve the momentum equation of porous media convection, i.e. (133) (instead we solved an Euler–Lagrange equation (26) which resembles (133) to some extent). The outcome of our analysis is the optimal steady flow, which might not satisfy (133). Solving the steady version of (132)–(134) in the limit of infinite Prandtl–Darcy number for one cell (using numerical continuation), Corson [5] has shown that $\mathrm{Nu} \sim \mathrm{Ra}^{2/3}$ and $\Gamma \sim \mathrm{Ra}^{-0.5}$. Furthermore, Corson [5] shows that if Γ is fixed, Nu scales as $\mathrm{Ra}^{1/3}$. Comparing these scalings with those obtained in the current work shows that steady convection in porous media does not transport as much as possible by a steady flow with a given amount of energy. This might be due to the fact that the flow in steady porous media convection differs significantly from the optimal steady flow (e.g. compare Figures 12b and 12a).

The latest direct numerical simulations (DNS) of (132)–(134) in the limit of infinite Prandtl–Darcy number at Ra as high as 4×10^4 show that Nu scales as Ra and that the cell aspect ratio scales as $\mathrm{Ra}^{-0.4}$ [9]. Comparing the steady [5] and unsteady [9] solutions of (132)–(134) suggests that unsteadiness might enhance the transport.

Table 1: Comparison of the results of the current work with the scalings for porous media convection obtained using various other methods.

	$\mathrm{Nu}(\mathrm{Ra})$	$\Gamma(\mathrm{Ra})$	$\mathrm{Nu}(\mathrm{Ra}, \Gamma_{\mathrm{fixed}})$
Boundary Layer Stability Argument			
Malkus [14], Howard [11], Horne & O'Sullivan [10]	$\sim C\,\mathrm{Ra}$		
Upper Bounds using Background Method			
Doering & Constantin [6]	$\leq 0.035\,\mathrm{Ra}$		
Otero *et al.* [16]	$\leq 0.029\,\mathrm{Ra}$		
Wen *et al.* [19]	$\lesssim 0.017\,\mathrm{Ra}$		
DNS: Unsteady Simulations			
Otero *et al.* [16]: $\mathrm{Ra} \leq 10^4$	$\sim C\,\mathrm{Ra}^{0.9}$		
Hewitt *et al.* [9]: $\mathrm{Ra} \leq 4 \times 10^4$	$\sim 0.007\,\mathrm{Ra}$	$\sim C\,\mathrm{Ra}^{-0.4}$	
Steady Unicellular Analysis			
Fowler [8]			$\sim C(\Gamma)\,\mathrm{Ra}^{1/3}$
Corson [5]	$\sim C\,\mathrm{Ra}^{2/3}$	$\sim C\,\mathrm{Ra}^{-0.5}$	$\sim C(\Gamma)\,\mathrm{Ra}^{1/3}$
Current Work			
Numerical & asymptotic analyses	$\leq 1 + 0.035\,\mathrm{Ra}$	$\sim 8.89\,\mathrm{Ra}^{-0.5}$	$\leq 1 + \frac{0.68}{\Gamma}\,\mathrm{Ra}^{0.5}$

Results of the current work show that the maximum possible steady transport scales linearly with Ra, which curiously agrees with the unsteady results. As shown in Figure 12, the optimal steady flow obtained here and the unsteady flow look similar to some extent. However, the unsteady transport is around 5 times smaller than the maximum possible steady transport at a given Ra, and the convection cells of the unsteady flow are wider than the optimal cells with aspect ratio Γ_{opt}.

3 Optimal Transport with Fixed Enstrophy

In the second problem, we investigate the optimal steady transport with fixed enstrophy. Therefore, equations (8)–(11) and (14) become

$$\mathbf{v} \cdot \nabla\theta = \Delta\theta + w, \tag{140}$$

$$\nabla \cdot \mathbf{v} = 0, \tag{141}$$

$$\mathrm{Pe} = \left\langle |\nabla \mathbf{v}|^2 \right\rangle, \tag{142}$$

$$\theta(x,0) = \theta(x,1) = 0, \tag{143}$$

$$w(x,0) = w(x,1) = 0. \tag{144}$$

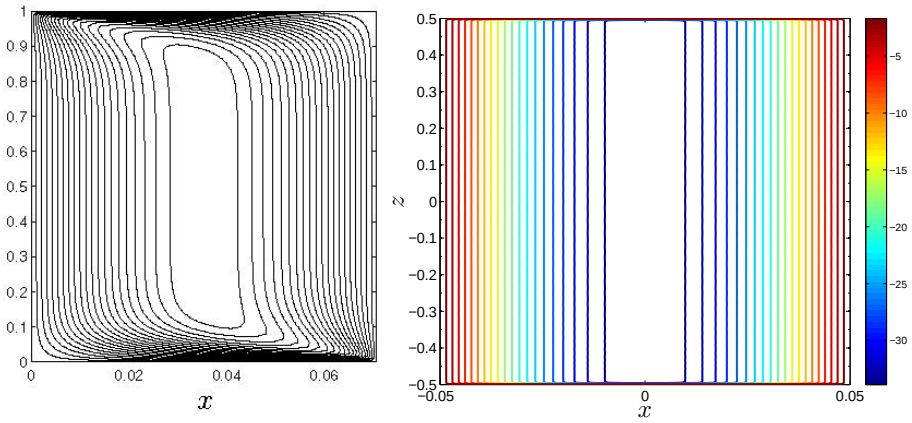

(a) (b)

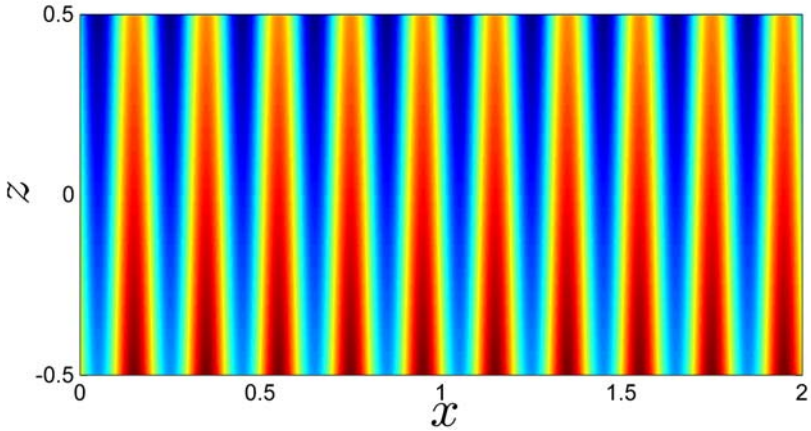

(c)

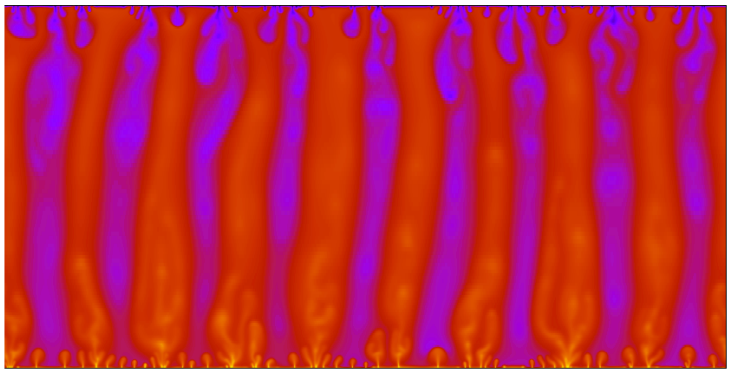

(d)

Figure 12: Streamfunction ψ for (a) steady porous media convection with $\Gamma = 0.07$ and $\mathrm{Ra} = 9976$ [5] and (b) steady optimal flow with $\Gamma = 0.1$ and $\mathrm{Ra} = 5658$. Temperature T in the large–Ra regime (c) steady optimal flow with $\Gamma = 0.1$ and $\mathrm{Ra} = 4028.4$ and (d) unsteady DNS results with $\mathrm{Ra} = 2 \times 10^4$ [9].

As for the first problem, a simple analysis gives a relatively crude upper bound of Nu. Starting from (16)

$$\begin{aligned}\mathrm{Nu} &= 1+\langle wT\rangle = 1+\langle w(T-1/2)\rangle \le 1+\left\langle |w|^2\right\rangle^{1/2}\left\langle |T-1/2|^2\right\rangle^{1/2} \le 1+\frac{\left\langle |\mathbf{v}|^2\right\rangle^{1/2}}{2}\\ &\le 1+\frac{\left\langle |\nabla\mathbf{v}|^2\right\rangle^{1/2}}{2\pi} = 1+\frac{\mathrm{Pe}}{2\pi},\end{aligned} \tag{145}$$

where as before, the Cauchy–Schwarz inequality and maximum principle have been used in the first line. The Poincaré inequality is applied to get the first term on the second line, and (142) is used to get the final result. This upper bound,is too high, and a full analysis of (140)–(144) is needed to obtain a better estimate. As the analysis is very similar to the first problem, many details are omitted for brevity.

3.1 Variational Formulation for Steady Flows

The variational formulation of the second problem involves maximizing equation (16) given constraints (140)–(142), and boundary conditions (143)-(144):

$$\mathcal{F} = \left\langle w\theta - \phi(x,z)\left(\mathbf{v}\cdot\nabla\theta - \Delta\theta - w\right) + p(x,z)\left(\nabla\cdot\mathbf{v}\right) + \frac{\mu}{2}\left(|\nabla\mathbf{v}|^2 - \mathrm{Pe}^2\right)\right\rangle, \tag{146}$$

where again, $\phi(x,z)$, $p(x,z)$, and μ are Lagrange multipliers. The Euler-Lagrange equations are:

$$0 = \frac{\delta\mathcal{F}}{\delta\mathbf{v}} = (\theta+\phi)\,\hat{\boldsymbol{z}} + \theta\,\nabla\phi - \nabla p + \mu\Delta\mathbf{v}, \tag{147}$$

$$0 = \frac{\delta\mathcal{F}}{\delta\theta} = \mathbf{v}\cdot\nabla\phi + \Delta\phi + w, \tag{148}$$

$$0 = \frac{\delta\mathcal{F}}{\delta\phi} = \mathbf{v}\cdot\nabla\theta - \Delta\theta - w, \tag{149}$$

$$0 = \frac{\delta\mathcal{F}}{\delta p} = \nabla\cdot\mathbf{v} \tag{150}$$

$$0 = \frac{\partial\mathcal{F}}{\partial\mu} = \left\langle|\nabla\mathbf{v}|^2\right\rangle - \mathrm{Pe}^2, \tag{151}$$

where again it has been assumed that ϕ vanishes at $z=[0,1]$. Also to eliminate the surface term $\nabla\cdot(\mathbf{v}\nabla\mathbf{v})$, we can use either the free–slip (i.e. $\partial u/\partial z = 0$) or no–slip (i.e. $u=0$) boundary conditions at $z=[0,1]$. Therefore the boundary conditions are the same as before, i.e.

$$w(x,0) = w(x,1) = 0, \tag{152}$$

$$\theta(x,0) = \theta(x,1) = 0, \tag{153}$$

$$\phi(x,0) = \phi(x,1) = 0, \tag{154}$$

in addition to one of

$$u(x,0) = u(x,1) = 0 \quad \mathrm{no-slip} \tag{155}$$

$$\left.\frac{\partial u}{\partial z}\right|_{z=0} = \left.\frac{\partial u}{\partial z}\right|_{z=1} = 0 \quad \mathrm{free-slip} \tag{156}$$

Here we only focus on the free–slip boundary condition and use (156).

Equations (147) and (149)-(150) look relatively similar to the Boussinesq equations (see e.g. [7]), although here, an extra field ϕ exists.

3.2 The Limit of Small Pe: Asymptotic Solution

In the limit of small Pe, $|\mathbf{v}| \ll 1$ and we can linearize equations (147)-(149):

$$
\begin{aligned}
-\mu\,\Delta\mathbf{v} + \nabla p &= (\theta+\phi)\hat{\boldsymbol{z}} && (157)\\
\Delta\phi + w &= 0, && (158)\\
\Delta\theta + w &= 0, && (159)\\
\nabla\cdot\mathbf{v} &= 0. && (160)
\end{aligned}
$$

Subtracting (159) from (158) and using (153)-(154) gives $\theta = \phi$ in the small–Pe regime. Taking the divergence of equation (157) and following the same steps as before results in

$$
-\mu\Delta\Delta w = 2\,\theta_{xx}, \tag{161}
$$

which along with equation (159), and boundary conditions (152)-(153) and (156) can be analytically solved to find ($\mathbf{v}$,θ) in the small–Pe limit.

A Fourier transform in the x direction, these equations become

$$
\begin{aligned}
(D_z^2 - k^2)\,\hat{\theta}_k(z) + \hat{w}_k(z) &= 0, && (162)\\
-\mu(D_z^2 - k^2)^2\,\hat{w}_k(z) + 2k^2\,\hat{\theta}_k(z) &= 0. && (163)
\end{aligned}
$$

As before, the solution has the form

$$
\begin{aligned}
\hat{w}_k(z) &= A_k\,\sin(m\pi z), && (164)\\
\hat{\theta}_k(z) &= B_k\,\sin(m\pi z), && (165)
\end{aligned}
$$

with unknown Fourier coefficients A_k and B_k. Substituting these equations into (162) and (163) gives

$$
\begin{aligned}
\mu &= (2\,k^2)/(m^2\pi^2 + k^2)^3, && (166)\\
A_k &= (m^2\pi^2 + k^2)\,B_k, && (167)
\end{aligned}
$$

and equation (160), yields

$$
\hat{u}_k(z) = i\,\frac{m\pi}{k}\,A_k\,\cos(m\pi z). \tag{168}
$$

Using (168) and (164) in (151) results in

$$
\left\langle |\nabla\mathbf{v}|^2 \right\rangle = \frac{1}{k^2}\left(m^2\pi^2 + k^2\right)^2 A_k^2 = \mathrm{Pe}^2 \Rightarrow A_k = \frac{k}{(m^2\pi^2 + k^2)}\,\mathrm{Pe}, \tag{169}
$$

which combined with (167) yields

$$
B_k = \frac{k}{(m^2\pi^2 + k^2)^2}\,\mathrm{Pe}. \tag{170}
$$

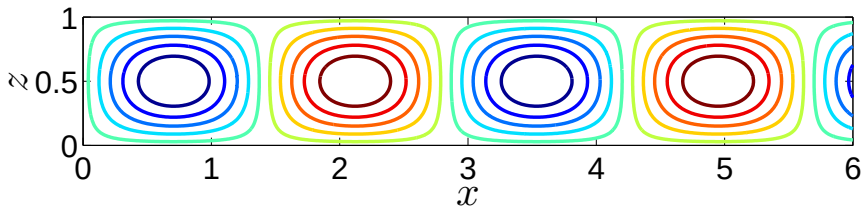

(a)

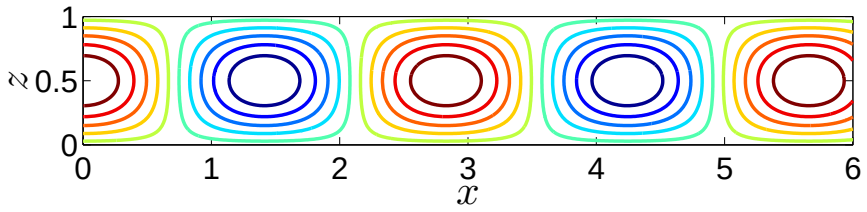

(b)

Figure 13: Optimal flow field in the small Pe limit for the fixed enstrophy problem with free-slip boundaries (a) streamlines ψ, (b) temperature θ.

Knowing A_k and B_k, Nu is obtained from (16):

$$\mathrm{Nu} = 1 + A_k B_k = 1 + \frac{k^2}{(m^2\pi^2 + k^2)^3}\,\mathrm{Pe}^2, \tag{171}$$

which for a given $(\mathrm{Pe}, \Gamma = \pi/k)$, is maximized at $m = 1$. As a result, using the notation defined in section 1.2:

$$\mathrm{Nu}_{\max}(\mathrm{Pe}, \Gamma) = 1 + \frac{\Gamma^4}{\pi^4(\Gamma^2 + 1)^3}\,\mathrm{Pe}^2. \tag{172}$$

The largest value of $\mathrm{Nu}_{\max}(\mathrm{Pe}, \Gamma)$, i.e. $\mathrm{Nu}_{\mathrm{MAX}}$, is achieved at $\Gamma_{\mathrm{opt}} = \sqrt{2}$:

$$\mathrm{Nu}_{\mathrm{MAX}}(\mathrm{Pe}) = 1 + \frac{\mathrm{Pe}^2}{(27\pi^4/4)}. \tag{173}$$

In the limit of small Pe, the maximum transport is achieved via an array of cells with aspect ratio $\Gamma_{\mathrm{opt}} = \sqrt{2}$ (Figure 13). This flow field (equations (164)–(165) and (168)), and the cells of the aspect ratio of $\sqrt{2}$, closely resemble those of the Rayleigh-Bénard convection (with free–slip boundary conditions) at the onset of linear instability (see e.g. [7]). The factor $27\pi^4/4$ in (173) is in fact the critical Ra of the instability.

3.3 Small to Large Pe: Numerical Simulation

Following the same steps as before, and using $\omega = \Delta\psi$, equations (147)-(150) simplify to

$$\begin{aligned}
\mathrm{J}(\theta, \phi) - \mu\,\Delta\omega + (\theta + \phi)_x &= 0, &(174)\\
\Delta\psi - \omega &= 0, &(175)\\
-\mathrm{J}(\psi, \theta) - \Delta\theta + \psi_x &= 0, &(176)\\
-\mathrm{J}(\psi, \phi) + \Delta\phi - \psi_x &= 0, &(177)
\end{aligned}$$

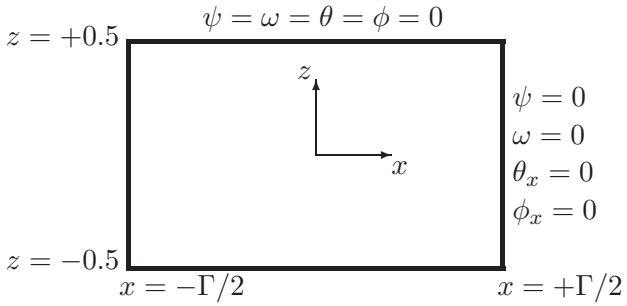

Figure 14: The fixed enstrophy problem: the geometry and boundary conditions of the computational domain which is a single 2D convection cell. Boundary conditions on the bottom (left) boundary are the same as top (right) boundary.

and boundary conditions (152)-(154) and (156) become

$$\psi(x,0) = \psi(x,1) = 0, \tag{178}$$
$$\omega(x,0) = \omega(x,1) = 0, \tag{179}$$
$$\theta(x,0) = \theta(x,1) = 0, \tag{180}$$
$$\phi(x,0) = \phi(x,1) = 0, \tag{181}$$

where ω has been introduced to avoid the occurrence fourth order derivatives and to simplify the implementation of boundary conditions.

Using the same continuation algorithm as given in section 2.3.1, and following the same steps as section 2.3.2 and appendix A, equations (174)-(177) become

$$\begin{bmatrix} \mu\Delta & -I & O & O \\ O & \mu\Delta & -(I+\phi_z^N)D_x + \phi_x^N D_z & -(I-\theta_z^N)D_x - \theta_x^N D_z \\ -(I-\theta_z^N)D_x - \theta_x^N D_z & O & \Delta - \psi_z^N D_x + \psi_x^N D_z & O \\ -(I+\phi_z^N)D_x + \phi_x^N D_z & O & O & \Delta + \psi_z^N D_x - \psi_x^N D_z \end{bmatrix} \begin{bmatrix} \delta\psi \\ \delta\omega \\ \delta\theta \\ \delta\phi \end{bmatrix}$$
$$= \begin{bmatrix} -\Delta\psi^N + \omega^N \\ -\mu\Delta\omega^N + (I+\phi_z^N)\theta_x^N + (I-\theta_z^N)\phi_x^N \\ -\Delta\theta^N + (I-\theta_z^N)\psi_x^N + \psi_z^N\theta_x^N \\ -\Delta\phi^N + (I+\phi_z^N)\psi_x^N - \psi_z^N\phi_x^N \end{bmatrix} \tag{182}$$

The details of the matrix algebra and boundary condition implementation are the same as before (see section 2.3.2).

3.3.1 Numerical Results

All the results presented here are obtained using $M = 61$ or 81. As before, the iterative solution always converged in less than 6 iterations, and the converged solution satisfies the equations and boundary conditions with the relative error of 10^{-10} or smaller.

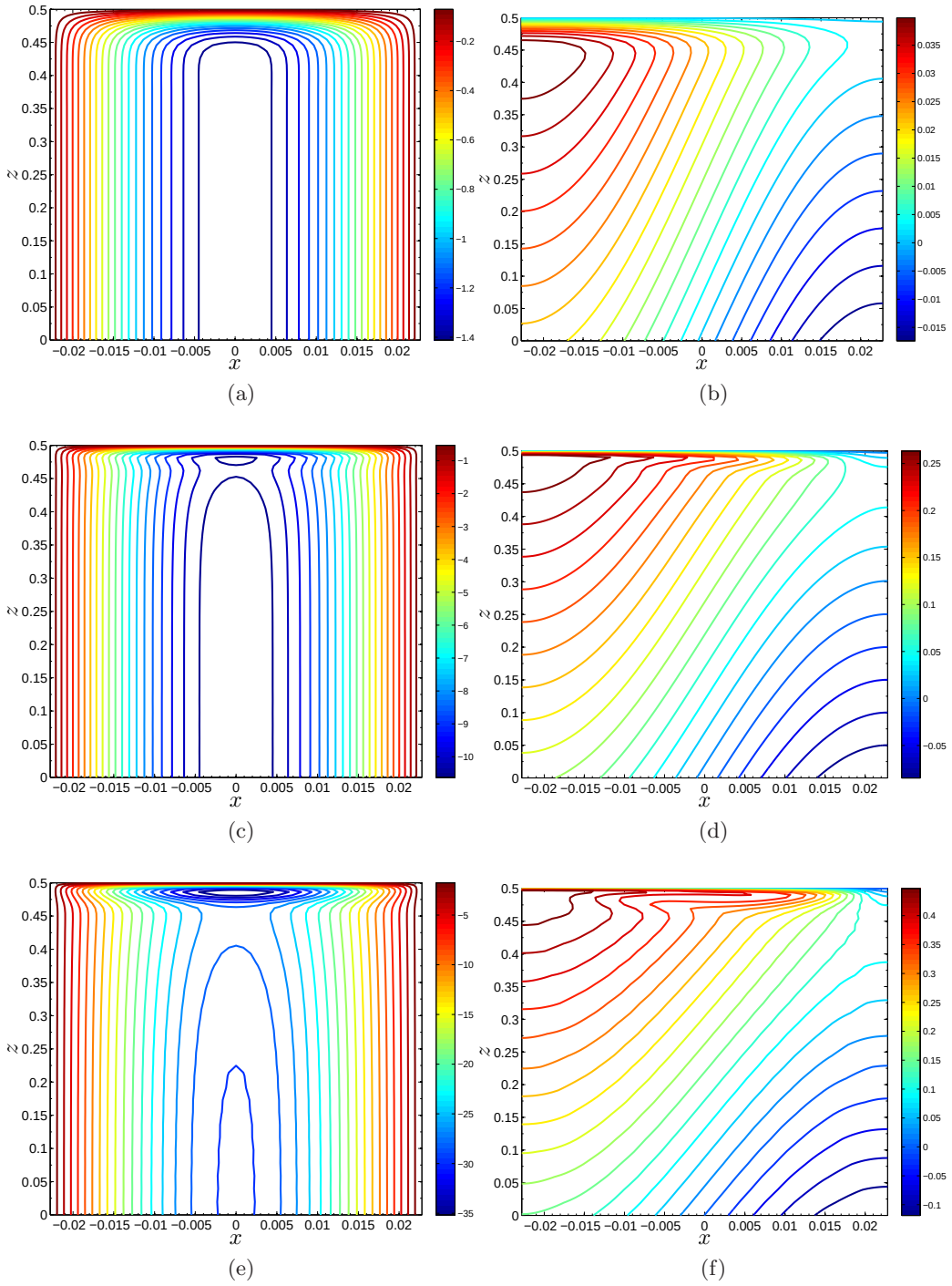

Figure 15: Evolution of the flow field with Pe for the case with $\Gamma = \sqrt{2}/\pi^3$. Panels on the left show ψ and panels on the right show θ (only the upper half of the domain is shown for better illustration of the circulation zone). (a) Pe = 4889.1, $\mathrm{Nu}_{\max} = 1.98$, (b) $\mathrm{Pe} = 3.97 \times 10^4$, $\mathrm{Nu}_{\max} = 40.1$, (c) $\mathrm{Pe} = 1.43 \times 10^5$, $\mathrm{Nu}_{\max} = 175.6$. The resolution is 81^2.

Figure 15 shows ψ and θ for the case with $\Gamma = \sqrt{2}/\pi^3$ for low to high values of Pe. $\mathrm{Nu}_{\max}$ increases withPe, and the flow structure changes. The enhancement of the heat transport is associated with the development of the boundary layers: the boundary layers thin as Pe increases and result in larger $\mathrm{Nu}_{\max}$. However, here we observe that for very large values of Pe, a circulation zone emerges between the boundary layers and the bulk. The circulation zone complicates the flow structure even for ξ and η. Figures 16 and 17 present $(\psi, \theta, \phi, \xi, \eta)$ for $\Gamma = \sqrt{2}/\pi^2$ and $\sqrt{2}/\pi^3$ in the limit of large Pe (the wiggles are due to the lack of numerical resolution). These results show that the optimal flow field for the fixed enstrophy problem is more complicated than the optimal flow field for the fixed energy problem, mainly due to the presence of the circulation zone. However, the bulk flows in the two problems still look rather similar: ψ and ξ are nearly independent of z and have a single mode dependence on x. η seems to be linear in z as before and nearly x–independent. Appendix C presents the interior solution for this problem:

$$\bar{\xi} = \pm\bar{\xi}_o \sin(\pi x/\Gamma), \tag{183}$$

$$\bar{\eta}_o = 2 - \left(\frac{\pi}{\Gamma}\right)^2 \sqrt{2\mu}, \tag{184}$$

$$\bar{\psi} = \frac{\pm\bar{\xi}_o}{(\pi/\Gamma)\sqrt{2\mu}} \cos(\pi x/\Gamma), \tag{185}$$

which agree with the observations of the numerical results. This solution is determined up to an unknown constant $\bar{\xi}_o$ which should be determined from the boundary layer solution. Owing to the complexity of this flow, we have not yet succeeded in solving the boundary layer equations and completing the matched asymptotic analysis.

In the absence of an analytical solution, we use the numerical results to find $\mathrm{Nu}_{\max}(\mathrm{Pe}, \Gamma)$ and $\mathrm{Nu}_{\mathrm{MAX}}(\mathrm{Pe})$. Figure 18 shows the numerically calculated $\mathrm{Nu}_{\max}(\mathrm{Pe}, \Gamma)$ for several values of Γ. The first three conclusions made from the results of Figure 6 are also true for these results. However, the scalings of $\mathrm{Nu}_{\max}$ and $\mathrm{Nu}_{\mathrm{MAX}}$ with Pe are different. For fixed Γ, we observe that

$$\mathrm{Nu}_{\max}(\mathrm{Pe}, \Gamma) = 1 + K(\Gamma)\,\mathrm{Pe}^{1/2}, \tag{186}$$

where $K(\Gamma)$ is a prefactor that can be determined from the numerical results. A fit to the envelope made by the largest values of $\mathrm{Nu}_{\max}$ gives

$$\mathrm{Nu}_{\mathrm{MAX}}(\mathrm{Pe}) = 1 + 0.2175\,\mathrm{Pe}^{10/17}. \tag{187}$$

The exponent we originally found by eyeballing was 0.58. However, the scaling of Nu with Ra reported by other investigators for Rayleigh–Bénard convection with stress–free boundaries (see Table 2) gives $\mathrm{Nu} \sim \mathrm{Ra}^{5/12}$. Interpreting their results in term of Pe (using (192) gives $\mathrm{Nu} \sim \mathrm{Pe}^{10/17=0.5882}$. This led us to believe that $\mathrm{Pe}^{10/17}$ is the scaling in our problem as well. Also note that this scaling is only valid for moderate and large values of Pe; in the limit of small Pe, (172) is the scaling of $\mathrm{Nu}_{\mathrm{MAX}}$. This explains the crossing of (187) and (145) in the limit of very small Pe.

To find $\Gamma_{\mathrm{opt}}(\mathrm{Pe})$ accurately from the numerical results, more data points in Γ (and especially for smaller Γ) are needed. However, using just three points in the wide range of $\mathrm{Pe} = 1701 - 4.1 \times 10^4$, we obtain -0.361 and -0.358 as the exponent of Pe in the scaling of $\Gamma_{\mathrm{opt}}(\mathrm{Pe})$.

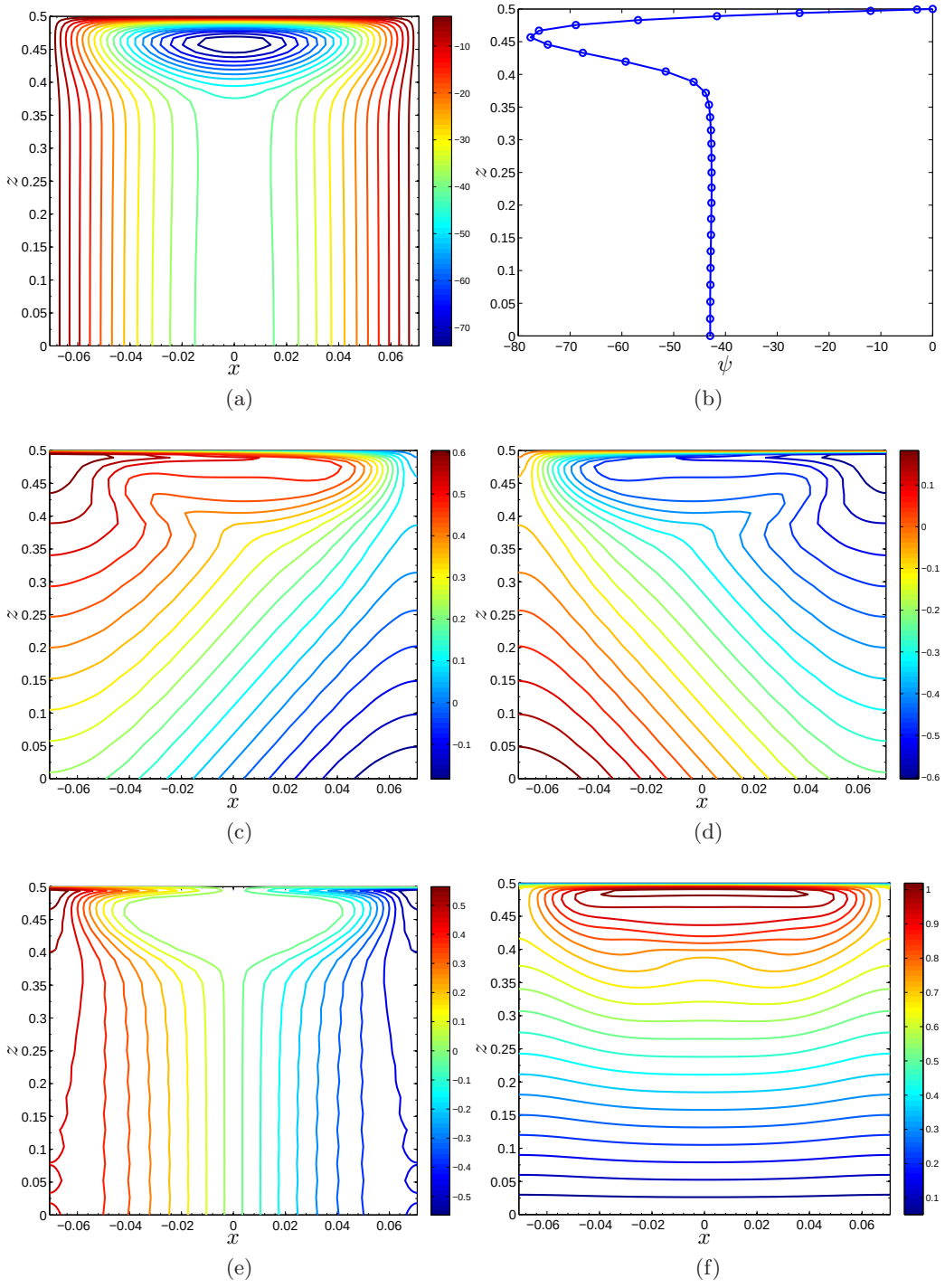

Figure 16: Flow field for $\Gamma = \sqrt{2}/\pi^2$, $\mu = 4.83\times10^{-8}$, $\mathrm{Pe} = 3.57\times10^4$, and $\mathrm{Nu}_{\max} = 103.3.7$. Only the upper half of the domain is shown for better illustration of the circulation zone. (a) ψ, (b) ψ along $x = 0$, (c) θ, (d) ϕ, (e) $\xi \equiv \theta + \phi$, and (f) $\eta \equiv \theta - \phi$. The resolution is 61^2.

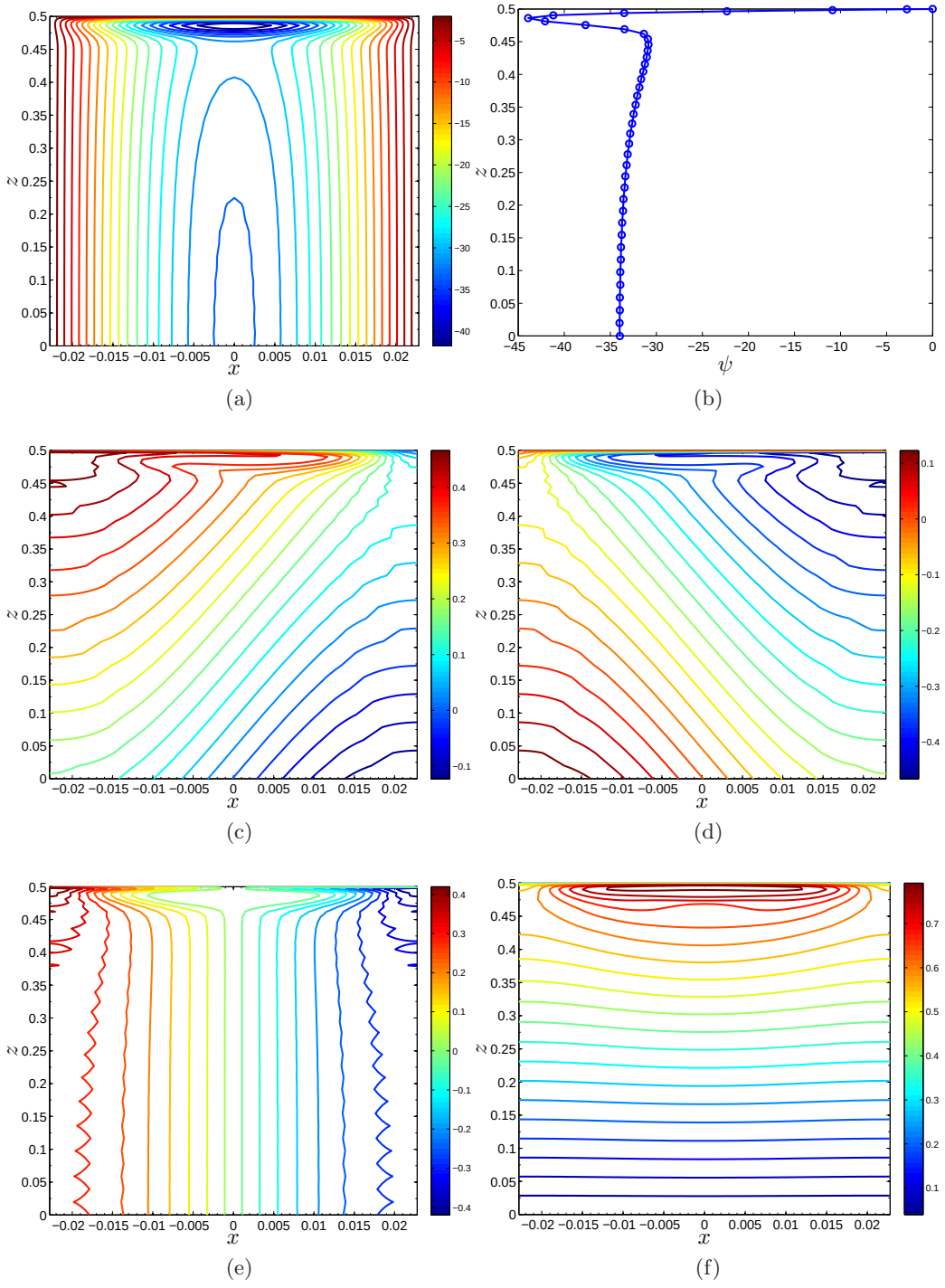

Figure 17: Flow field for $\Gamma = \sqrt{2}/\pi^3$, $\mu = 9.7 \times 10^{-9}$, $\mathrm{Pe} = 1.2 \times 10^5$, and $\mathrm{Nu}_{\max} = 153.1$. Only the upper half of the domain is shown for better illustration of the circulation zone. (a) ψ, (b) ψ along $x = 0$, (c) θ, (d) ϕ, (e) $\xi \equiv \theta + \phi$, and (f) $\eta \equiv \theta - \phi$. The resolution is 81^2.

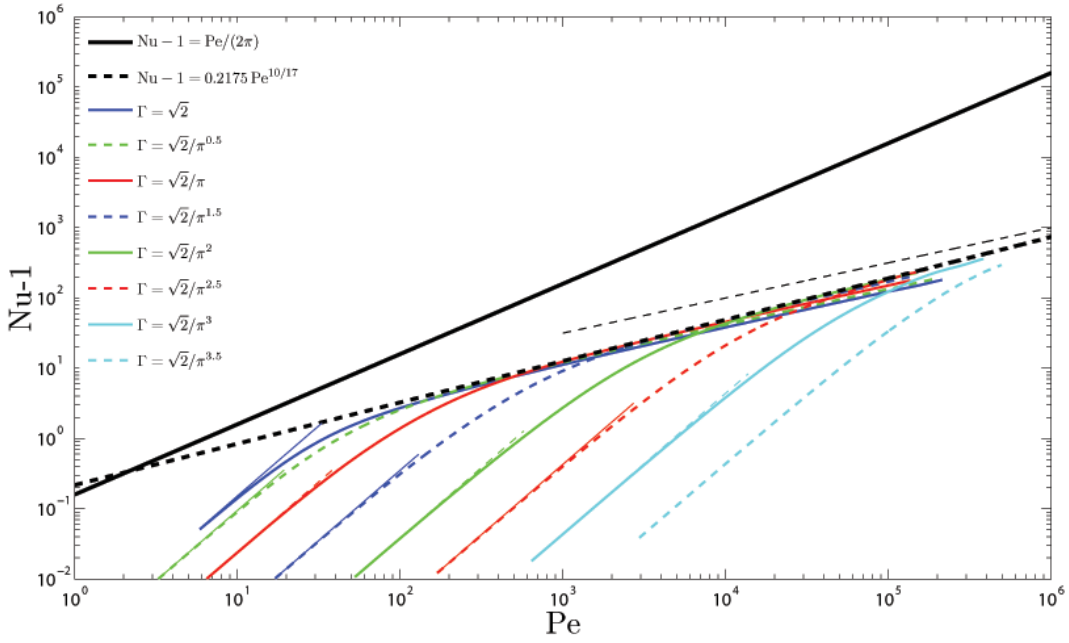

Figure 18: The non-black lines show the numerically obtained $\mathrm{Nu}_{\max}$ as a function of Pe for various values of Γ. For each case, the thin short line of the same color, visible for most of the cases, shows the analytical $\mathrm{Nu}_{\max}$ (172) in the limit of small Pe. The thick solid black line shows the absolute upper bound (145), and the thick broken black line shows a fit to the envelope (i.e. $\mathrm{Nu}_{\mathrm{MAX}}$) (see equation (187)). The thin broken black line indicates the $\mathrm{Pe}^{1/2}$ slope. All numerical results started with linear solutions with $m = 1$ and all results shown here have resolution $M = 61$. Using a higher resolution $M = 81$ results in negligible changes to the plot.

3.4 Example: Application to Rayleigh-Bénard Convection

Rayleigh-Bénard convection, i.e. convection in a layer of fluid heated from below and cooled from above, is a problem of great interest in science and engineering and has been studied extensively over the past few decades [1]. Here we show that this problem is an example of transport with fixed enstrophy. We find $\mathrm{Nu}_{\max}$ and $\mathrm{Nu}_{\mathrm{MAX}}$ as a function of the Rayleigh number Ra and compare them with the results of previous analytical and numerical analyses.

Rayleigh-Bénard convection is modeled by the Boussinesq equations [7, 20]:

$$\nabla \cdot \mathbf{v} = 0, \tag{188}$$

$$\frac{1}{\mathrm{Pr}}\left(\dot{\mathbf{v}} + \mathbf{v}\cdot\nabla\mathbf{v}\right) = -\nabla p + \Delta\mathbf{v} + \mathrm{Ra}\,T\mathbf{z}, \tag{189}$$

$$\dot{T} + \mathbf{v}\cdot\nabla T = \Delta T, \tag{190}$$

where Pr is the Prandtl number.

Multiplying (189) by $\mathbf{v}$ and integrating over long time and over a domain with impermeable walls gives

$$0 = \left\langle |\nabla\mathbf{v}|^2 \right\rangle + \mathrm{Ra}\,\langle wT\rangle\,, \tag{191}$$

where the left–hand side and the pressure term vanish due to the long time–space averaging. Using the definition of Pe for the fixed enstrophy problems (14) and Nu (16) from section 1.1 we obtain

$$\mathrm{Pe}^2 = \mathrm{Ra}\,(\mathrm{Nu}-1). \tag{192}$$

As argued before, the Nusselt number Nu, when calculated by long–time averaging, is just a function of Ra. As a result, in both steady and statistically–steady flows, equation (192) shows that Pe is fixed for a fixed value of Ra (as before Ra depends on the fluid properties and the imposed temperature difference between the walls; it does not depend on the flow). Therefore, Rayleigh-Bénard convection occurs with fixed enstrophy. Employing the analogy made before between enstrophy and viscous dissipation in (4), we can conclude that Rayleigh-Bénard convection in Newtonian fluids occurs with fixed viscous dissipation.

Employing (192), Pe can be replaced with Ra in (186) and (187):

$$\mathrm{Nu}_{\max}(\mathrm{Ra},\Gamma) = 1 + (K(\Gamma))^{4/3}\,\mathrm{Ra}^{1/3}, \tag{193}$$

$$\mathrm{Nu}_{\mathrm{MAX}}(\mathrm{Ra}) = 1 + 0.1152\,\mathrm{Ra}^{5/12}. \tag{194}$$

Also using the rather crude approximations we obtained for the exponent of Pe in $\Gamma_{\mathrm{opt}}(\mathrm{Pe})$,

$$\Gamma_{\mathrm{opt}}(\mathrm{Ra}) \sim \mathrm{Ra}^{-0.2546}. \tag{195}$$

Curiously, $\mathrm{Ra}^{-0.25}$ is the scaling of the smallest unstable mode for Rayleigh-Bénard convection (the same agreement was observed for porous media convection, see equation (139)).

Table 2 compares (193)–(194) with the results obtained using other methods in the literature. The classical argument of Malkus [14] and Howard [11], which is based on the marginal stability of the boundary layer, gives $\mathrm{Nu} \sim \mathrm{Ra}^{1/3}$ while the argument by Spiegel [17] and Kraichnan [13] gives $\mathrm{Nu} \sim \mathrm{Ra}^{1/2}$. These arguments are independent of the type

Table 2: Comparison of the results of the current work with the scalings for Rayleigh–Bénard convection with free–slip boundary condition obtained using various other methods.

	$\mathrm{Nu}(\mathrm{Ra},\mathrm{Pr})$	$\mathrm{Nu}(\mathrm{Ra},\Gamma_{\mathrm{fixed}})$
Classical Theories		
Malkus [14] & Howard [11]	$\sim C\,\mathrm{Ra}^{1/3}$	
Spiegel [17] & Kraichnan [13]	$\sim C\,(\mathrm{Pr}\ \mathrm{Ra})^{1/2}$	
Upper Bounds using Background Method		
Ierley *et al.* [12]: Numerical with infinite Pr	$\leq C\,\mathrm{Ra}^{5/12}$	
Otero *et al.* [15]: 2D Numerical with finite Pr	$\leq 0.142\,\mathrm{Ra}^{5/12}$	
Whitehead & Doering [20]:	$\leq 0.289\,\mathrm{Ra}^{5/12}$	
Analytical, 2D finite Pr and 3D infinite Pr)		
DNS: Unsteady Turbulent Simulations	inconclusive	
Steady Unicellular Analysis		
Chini & Cox [4]		$\sim C(\Gamma)\,\mathrm{Ra}^{1/3}$
Current Work:		
Numerical	$\leq 1 + 0.115\,\mathrm{Ra}^{5/12}$	$\leq 1 + (K(\Gamma))^{4/3}\,\mathrm{Ra}^{1/3}$

of boundary conditions. For free–slip boundary conditions, the background method gives $\mathrm{Nu} \sim \mathrm{Ra}^{5/12}$ independent of the Pr number [12, 15, 20]. DNS results of (188)–(190) for high–Ra turbulent convection with free-slip boundary conditions, conducted by several research groups, are still inconclusive.

$\mathrm{Nu}_{\mathrm{MAX}}(\mathrm{Ra})$ obtained in this work has the same scaling in Ra as the upper bounds obtained using the background method. This was also the case for the fixed energy problem. For fixed Γ, Chini and Cox [4] have analyzed the steady Rayleigh–Bénard connection in one cell (in an approach very similar to the current work) and found that $\mathrm{Nu} \sim \mathrm{Ra}^{1/3}$, which agrees with the scaling of $\mathrm{Nu}_{\mathrm{max}}(\mathrm{Ra},\Gamma)$ with Ra obtained here. This agreement suggests that steady Rayleigh–Bénard convection transports as much as possible by a steady flow with a given amount of enstrophy, modulo a constant prefactor.

4 Concluding Remarks

How much heat can be transported by flows which have a given amount of kinetic energy or enstrophy? What the optimal velocity field look like? In this investigation, we addressed these questions for steady incompressible 2D flows. We focused on heat transport between two parallel impermeable walls. For each of the two main constraints (fixed kinetic energy and fixed enstrophy), we employed the calculus of variations to find the divergence-free velocity field that maximizes the heat transport between the walls. We solved the resulting nonlinear Euler-Lagrange equations numerically in a cell of a given aspect ratio Γ. For the problem with fixed kinetic energy, we exploited the symmetries in the flow and solved the nonlinear equations using matched asymptotic analysis as well. The analytical and numerical results agree remarkably well. The problem could be readily formulated for mass transport, or the transport of any scalar tracer.

We report our results based on Nusselt number Nu and Péclect number Pe, which

quantify the heat transport and the strength of advection, respectively. For both problems, our analysis shows that as Pe increases, the maximum possible transport $\mathrm{Nu}_{\mathrm{MAX}}$ is achieved by cells of smaller aspect ratio. For the problem with fixed energy, we found that $\mathrm{Nu}_{\mathrm{MAX}} \sim \mathrm{Pe}$ and $\Gamma_{\mathrm{opt}} \sim \mathrm{Pe}^{-0.5}$. If enstrophy is fixed, $\mathrm{Nu}_{\mathrm{MAX}} \sim \mathrm{Pe}^{10/17}$ and $\Gamma_{\mathrm{opt}} \sim \mathrm{Pe}^{-0.36}$.

For practical purposes, we assume that the optimal velocity field can be produced by a combination of force fields, although such a flow might be linearly or nonlinearly unstable. For each of the two main constraints, we have looked into a buoyancy-driven flow which satisfies that constraint to see how the transport compares with upper bounds. For these problems we interpret the results in terms of the Ra number which is more appropriate. For convection in porous media, which occurs with fixed energy, we have found $\mathrm{Nu}_{\mathrm{MAX}} \sim \mathrm{Ra}$ and $\Gamma_{\mathrm{opt}} \sim \mathrm{Ra}^{-0.5}$. For Rayleigh-Bénard convection, an example of fixed enstrophy transport, we found $\mathrm{Nu}_{\mathrm{MAX}} \sim \mathrm{Ra}^{5/12}$ and $\Gamma_{\mathrm{opt}} \sim \mathrm{Ra}^{-0.25}$. Interestingly, for both problems the scalings of $\Gamma_{\mathrm{opt}}(\mathrm{Ra})$ agree with the scalings of the smallest unstable mode.

The research presented in this work gives new insight into steady 2D optimal transport. There are several lines of research which should be pursued to further expand our understanding of optimal transport:

- Completing the large–Pe asymptotic solution for the fixed enstrophy problem would help in confirming and interpreting the numerical results
- Studying the fixed enstrophy problem with no-slip boundary conditions is more challenging but of great interest
- Obtaining conclusive results for the unsteady turbulent simulation and steady unicellular analysis of the Rayleigh–Bénard problem with free- and no-slip boundary conditions and for small and high values of Pr number would significantly improve our understanding of the physics of heat transport
- Investigating the transport by 3D cells, although difficult, should produce interesting results
- Finally, studying unsteady transport using optimal control is of great interest and importance and will result in much deeper insight into turbulent transport

Acknowledgments

I am deeply grateful to Charlie Doering and Greg Chini for proposing this project and for insightfully guiding me through the summer. Their devotion, patience, and support made this project a productive and enjoyable experience. I would like to express my gratitude toward the faculty, staff, and participants of the 2012 GFD program, especially George Veronis and Colm Caulfield, for the inspiring and fruitful summer. Particularly, I would like to thank all the fellows for the great time we had in Walsh Cottage, softball field, and Captain Kidd. Special thanks are extended to Duncan Hewitt for answering my questions about porous media convection, and Cédric Baume for our informative discussions about numerics. I appreciate Lindsey Corson's kind support at the beginning of the summer.

Also I would like to thank Phil Marcus for teaching me computation and analytical methods, which I used throughout this work. Furthermore, I am thankful to John Neu for his wonderful course on asymptotic analysis which I greatly benefited from during this project.

A Equations for Newton-Kantorovich Iteration Scheme

Here we present more details on how equation (67) was derived. First, we deduce from equations (53)-(55) that

$$\begin{aligned} \mathrm{F} &= \frac{1}{\mu}\left(-(1+\phi_z)\theta_x + (\theta_z-1)\phi_x\right), && (196)\\ \mathrm{G} &= (1-\theta_z)\psi_x + \psi_z\theta_x, && (197)\\ \mathrm{Q} &= (1+\phi_z)\psi_x - \psi_z\phi_x. && (198) \end{aligned}$$

Calculating the Frechet derivatives, recalling the definition of $\delta(\cdot) \equiv (\cdot)^{N+1} - (\cdot)^N$, and ignoring the higher order terms, equations (64)-(66) become

$$\begin{aligned} \mu\Delta\delta\psi + (1+\phi_z^N)\,\delta\theta_x - \phi_x^N\,\delta\theta_z + (1-\theta_z^N)\,\delta\phi_x + \theta_x^N\,\delta\phi_z &= \\ -\mu\Delta\psi^N - \left[(1+\phi_z^N)\theta_x^N + (1-\theta_z^N)\phi_x^N\right] && (199)\\ \Delta\delta\theta - \psi_z^N\,\delta\theta_x + \psi_x^N\,\delta\theta_z - (1-\theta_z^N)\,\delta\psi_x - \theta_x^N\,\delta\psi_z &= \\ -\Delta\theta^N + (1-\theta_z^N)\psi_x^N + \psi_z^N\theta_x^N && (200)\\ \Delta\delta\phi - (1+\phi_z^N)\,\delta\psi_x + \phi_x^N\,\delta\psi_z + \psi_z^N\,\delta\phi_x - \psi_x^N\,\delta\phi_z &= \\ -\Delta\phi^N + (1+\phi_z^N)\psi_x^N - \psi_z^N\phi_x^N && (201) \end{aligned}$$

B Limit of $\lambda \ll 1$ and $\sigma \ll 1$

To study the large Pe asymptotic solution in the case that $\sigma \ll 1$, we start from equations (96)-(98). The main difference between the current analysis and the one in section 2.4.2 is that the $(2-\pi\sqrt{2\mu}/\Gamma)$ term is $\mathcal{O}(1/\Gamma) \gg 1$ if $\sigma \ll 1$ (as opposed to $\mathcal{O}(1)$ in section 2.4.2). Therefore, it contributes to the balancing of the leading order. Only keeping the terms which might contribute to the leading order, and rearranging a few constants, we get

$$\begin{aligned} \left[-\pi^2 A + \frac{\Gamma^2}{\delta_1^2}A''\right] - \frac{\pi^2}{2\delta_3}C'\,B &= 0, && (202)\\ -\frac{\mu}{\delta_3^2}C'' + \frac{\bar{\xi}_o^2}{2}\left[\frac{1}{\delta_2}AB' + \frac{1}{\delta_1}BA'\right] &= 0, && (203)\\ \left[-\pi^2 B + \frac{\Gamma^2}{\delta_2^2}B''\right] - \frac{\pi^2}{2\delta_3}C'\,A &= 0. && (204) \end{aligned}$$

The first equation shows that the same as section 2.4.2, the balance is between the A'' and $C'\,B$ terms and $\delta_1^2 = \Gamma^2\delta_3$. Similarly, in the third equation the balance is between B'' and $C'\,A$ terms and $\delta_2^2 = \Gamma^2\delta_3$, implying that $\delta_1 = \delta_2$. The balancing terms in the second equation are the same as before as well, and $\delta_3^2 = \mu\delta_1$. Combining these equalities gives

$$\begin{aligned} \delta_1 = \delta_2 &= \Gamma^{4/3}\,\mu^{1/3}, && (205)\\ \delta_3 &= \Gamma^{2/3}\,\mu^{2/3}. && (206) \end{aligned}$$

Therefore, unlike section 2.4.2, here ψ and ξ do not have the same boundary layer thickness as η which complicates the problem as we have to deal with a nested boundary layer.

However, the $\mathrm{Nu}_{\max}(\mathrm{Pe})$ obtained in section 2.4.5 agrees very well with the results of the numerical simulations (see Figure 6) and shows that the optimal transport is achieved in the distinguished limit that $\sigma = \mathcal{O}(1)$. Therefore, we do not further analyze the $\sigma \ll 1$ limit.

C Interior Solution for the Fixed Enstrophy Problem

Equations (174) and (177)-(176) can be written in terms of (ψ, ξ, η)

$$
\begin{aligned}
-\mathrm{J}(\xi,\eta) - 2\mu\Delta^2\psi + 2\xi_x &= 0, && (207)\\
\mathrm{J}(\psi,\xi) + \Delta\eta &= 0, && (208)\\
\mathrm{J}(\psi,\eta) + \Delta\xi - 2\psi_x &= 0, && (209)
\end{aligned}
$$

which except for $-2\mu\Delta^2$ instead of $+2\mu\Delta$ are the same as (70)-(72). However, the higher derivative is expected to result in major differences between the two problems.

The numerical results suggests

$$
\begin{aligned}
\psi &= \bar{\psi}(x)\, A(x,z), && (210)\\
\xi &= \bar{\xi}(x)\, B(x,z), && (211)\\
\eta &= \bar{\eta}(z)\, C(x,z), && (212)
\end{aligned}
$$

where $(\bar{\psi}, \bar{\xi}, \bar{\eta})$ constitute the outer solution.

Using $(\bar{\psi}(x)$,$\bar{\xi}(x)$,$\bar{\eta}(z))$ in (207)-(209) gives

$$
\begin{aligned}
2\mu\,\bar{\psi}_{xxxx} - (2-\bar{\eta}_z)\,\bar{\xi}_x &= 0, && (213)\\
\bar{\eta}_{zz} &= 0, && (214)\\
\bar{\xi}_{xx} - (2-\bar{\eta}_z)\bar{\psi}_x &= 0, && (215)
\end{aligned}
$$

which again imply that

$$
\bar{\eta}(z) = \bar{\eta}_o\, z, \qquad (216)
$$

where $\bar{\eta}_o$ is an unknown constant. Eliminating $\bar{\psi}$ between (213) and (215) yields

$$
\bar{\xi}_{xxxxx} - \left(\frac{\bar{\eta}_o - 2}{\sqrt{2\mu}}\right)^2 \bar{\xi}_x = 0, \qquad (217)
$$

Given the periodicity of 2Γ in x, and $\xi_x(\pm\Gamma/2, z) = 0$, this implies

$$
\begin{aligned}
\bar{\xi} &= \pm\bar{\xi}_o \sin(\pi\, x/\Gamma) && (218)\\
\bar{\eta}_o &= 2 - \left(\frac{\pi}{\Gamma}\right)^2 \sqrt{2\mu}, && (219)
\end{aligned}
$$

where $\bar{\xi}_o > 0$ is an unknown constant. Notice the difference between (219) and 85).

Equation (215) yields

$$
\bar{\psi} = \frac{\pm\bar{\xi}_o}{(\pi/\Gamma)\sqrt{2\mu}} \cos(\pi\, x/\Gamma). \qquad (220)
$$

As before, the interior flow field (i.e. outer solution) is known up to an unknown constant $\bar{\xi}_o$ which shall be determined using the inner solution.

References

[1] G. Ahlers, S. Grossmann, and D. Lohse, *Heat transfer and large scale dynamics in turbulent Rayleigh–Bénard convection*, Review of Modern Physics, 81 (2009).

[2] G. B. Arfken and H. J. Weber, *Mathematical Methods for Physicists*, Academic Press, 6th ed., 2005.

[3] J. P. Boyd, *Chebyshev and Fourier Spectral Methods*, Dover, 2nd ed., 2001.

[4] G. P. Chini and S. M. Cox, *Large Rayleigh number thermal convection: heat flux predictions and strongly nonlinear solutions*, Physics of Fluids, 21 (2009).

[5] L. T. Corson, *Maximizing the heat flux in steady unicellular porous media convection*, Geophysical Fluid Dynamics Program Report, Woods Hole Oceanographic Institution, (2011).

[6] C. R. Doering and P. Constantin, *Bounds for heat transport in a porous layer*, Journal of Fluid Mechanics, 376 (1998).

[7] P. G. Drazin and W. H. Reid, *Hydrodynamic Stability*, Cambridge University Press, 2nd ed., 2004.

[8] A. C. Fowler, *Mathematical Models in the Applied Sciences*, Cambridge University Press, 1st ed., 1997.

[9] D. R. Hewitt, J. A. Neufeld, and J. R. Lister, *Ultimate regime of high Rayleigh number convection in a porous medium*, Physical Review Letters, 108 (2012).

[10] R. N. Horne and P. O'Sullivan, *Origin of oscillatory convection in a porous medium heated from below*, Physics of Fluids, 21 (1978).

[11] L. Howard, *Convection at high Rayleigh numbers*, Proceedings of the 11th International Congress of Applied Mechanics, edited by H. Görtler (1964).

[12] G. R. Ierley, R. R. Kerswell, and S. C. Plasting, *Infinite–prandtl–number convection. part 2. a singular limit of upper bound theory*, Journal of Fluid Mechanics.

[13] R. H. Kraichnan, *Turbulent thermal convection at arbitrary Prandtl number*, Physics of Fluids, 5 (1962).

[14] W. V. R. Malkus, *The heat transport and spectrum of thermal turbulence*, Proceedings of the Royal Society of London. Series A, 225 (1954).

[15] J. Otero, *Bounds for the heat transport in turbulent convection*, Ph.D. Thesis, University of Michigan, 2002.

[16] J. Otero, L. A. Dontcheva, H. Johnston, R. A. Worthing, A. Kurganov, G. Petrova, and C. R. Doering, *High–Rayleigh–number convection in a fluid–saturated porous layer*, Journal of Fluid Mechanics, 500 (2004).

[17] E. A. Spiegel, *Thermal turbulence at very small Prandtl number*, Journal of Geophysical Research, 67 (1962).

[18] L. N. Trefethen, *Spectral Methods in MATLAB*, SIAM, 1st ed., 2001.

[19] B. Wen, N. Dianati, E. Lunasin, G. P. Chini, and C. R. Doering, *New upper bounds and reduced dynamical modeling for Rayleigh-Bénard convection in a fluid saturated porous layer*, Journal of Fluid Mechanics, 500 (2004).

[20] J. P. Whitehead and C. R. Doering, *Ultimate state of two–dimensional Rayleigh–Bénard convection between free–slip fixed–temperature boundaries*, Physical Review Letters, 106 (2011).